

An Analysis of Peristaltic Locomotion for Maximizing Velocity or Minimizing Cost of Transport of Earthworm-Like Robots

Akhil Kandhari,¹ Yifan Wang,¹ Hillel J. Chiel,²⁻⁴ Roger D. Quinn,¹ and Kathryn A. Daltorio¹

Abstract

Earthworm-like peristaltic locomotion has been implemented in >50 robots, with many potential applications in otherwise inaccessible terrain. Design guidelines for peristaltic locomotion have come from observations of biology, but robots have empirically explored different structures, actuators, and control waveform shapes than those observed in biological organisms. In this study, we suggest a template analysis based on simplified segments undergoing beam deformations. This analysis enables calculation of the minimum power required by the structure for locomotion and maximum speed of locomotion. Thus, design relationships are shown that apply to peristaltic robots and potentially to earthworms. Specifically, although speed is maximized by moving as many segments as possible, cost of transport (COT) is optimized by moving fewer segments. Furthermore, either soft or relatively stiff segments are possible, but the anisotropy of the stiffnesses is important. Experimentally, we show on our earthworm robot that this method predicts which control waveforms (equivalent to different gaits) correspond to least input power or to maximum velocity. We extend our analysis to 150 segments (similar to that of earthworms) to show that reducing COT is an alternate explanation for why earthworms have so few moving segments. The mathematical relationships developed here between structural properties, actuation power, and waveform shape will enable the design of future robots with more segments and limited onboard power.

Keywords: peristaltic locomotion, earthworm-like robot, biologically inspired robots

Introduction

EARTHWORM ROBOTS are deceptively simple, making them a promising and interesting type of soft robot. Each segment of an earthworm's body is radially symmetric and approximately identical, which makes it convenient for modular design at various length scales. Instead of discrete feet, earthworm robots can use their entire body surface for traction, which can be increased by material softness. As a result, earthworm-like robots have been suggested for many soft robotic applications, such as search and rescue operations,¹ underground exploration,²⁻⁴ pipe inspection,^{5,6} and medical procedures such as endoscopy or colonoscopy.⁷⁻⁹

However, despite this apparent simplicity, design remains nontrivial. Throughout the animal kingdom, peristaltic locomotion is ubiquitous (e.g., in larval stages and in adults¹⁰), and some worm-like organisms are capable of rapid¹¹ and

precise¹² movements. In contrast, although >50 earthworm-like mobile robots (Fig. 1) have been implemented, it has proven surprisingly challenging to achieve the effective motion observed in biological organisms. Several specific challenges have been identified, including stiffness optimization,^{13,14} loss of power efficiency due to slip,^{15,16} and precise control of soft segments, which may vary both in their fabrication and over time.¹⁷ Indeed, it is entirely possible to construct a series of worm-like segments that, when assembled, do not locomote satisfactorily. Both structural properties and gait selection are key to coordinated locomotion. Often it is possible to empirically optimize segment structure or control to improve results, but an analytical guide could help designers to decide fundamental questions about actuation, structure, control, and sensing for soft peristaltic devices.

In this study, we clarify how the essential characteristics in peristaltic locomotion (actuation, control, and softness)

Departments of ¹Mechanical and Aerospace Engineering, ²Biology, ³Neurosciences and ⁴Biomedical Engineering, Case Western Reserve University, Cleveland, Ohio, USA.

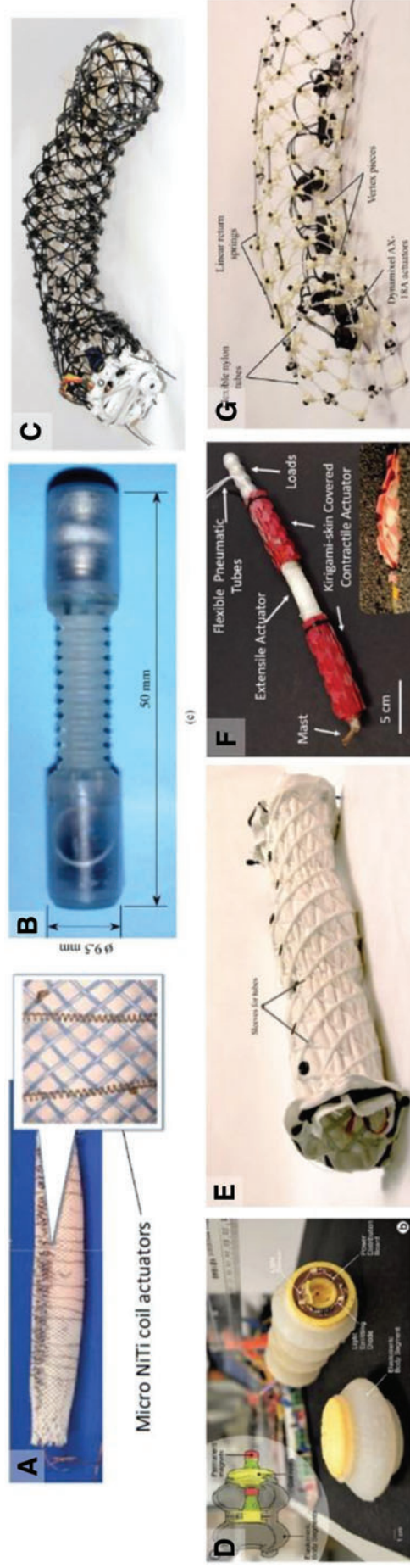


FIG. 1. Recent worm-like robots. (A) Meshworm,⁴¹ an expandable nylon mesh using shape memory alloy (Nitinol) for actuation. (B) Peristaltic micro robot composed of silicone bellows that is capable of deforming using Nitinol and undergoes the “two-anchor method” of peristaltic locomotion.¹³ (C) Softworm,¹⁵ a cable actuated peristaltic robot made of flexible cables and pinned joints. (D) A modular worm-like robot,⁹⁷ which utilizes voice coils, connected by flexible silicone membranes for actuation. (E) A peristaltic crawling robot actuated using servomotor and a fabric-integrated-mesh.⁹⁴ (F) Soft worm-like robot that models the putative earthworm anchoring mechanism by combining kirigami skin with radially expanding pneumatic actuators.⁵⁷ (G) Compliant Modular Mesh Worm with Steering (CMMWorm-S),¹⁴ a cable actuated modular worm-like robot capable of turning. *(A) and (F) reproduced with permission from IEEE, (B) reproduced with permission from Elsevier, and (D) reproduced with permission from Mary Ann Liebert, Inc. Color images are available online.

contribute to the design of earthworm-like robots. Previously, textbook models of worm locomotion claimed that the ratio of moving to anchoring segments is limited by differences in forward and backward friction coefficients.¹⁸ This would explain observations of biological earthworms in which about equal numbers of segments are moving and anchoring at any given time.¹⁹ However, by requiring slip against anisotropic friction, this explanation contradicts experience with engineered worm robots, which often have minimal anchoring segments and use isotropic friction.^{3,4,13} Minimizing the number of anchoring segments increases speed, whereas isotropic friction allows a robot to reverse its direction and extract itself from the environment. Thus, more accurate design constraints are needed for robotics applications.

Our study builds on previous researchers' mathematical models for peristaltic locomotion that are specific to either earthworms or earthworm-like robots. Chapman²⁰ described the nonlinear kinematic relationship between the length and diameter of a segment of an earthworm assuming a constant hydrostatic volume. For muscular hydrostats specifically, it has been shown that the resulting mechanical advantage allows longitudinal muscles to be stronger at longer structure lengths, and for circumferential muscles to be effective antagonists at shorter structure lengths.²¹ Our prior study has characterized mesh kinematics and compared it with constant volume constraints.¹⁷ In this article, we rely on a simpler linearization in the form of Poisson's ratio to generalize to a wider array of robots.

Previously, Jiang and Xu²² considered small-scale robots in a viscous medium. Using a reduced dynamic model, the authors correlated locomotion performance to wave and structural parameters such as distance between two adjacent waves, wave width, and body length. These results correlate with empirical velocity optimization of a robot in a dry acrylic tube.²³ In this study, we also factor in soft deformation due to gravity and consider energetic efficiency as well as total speed. Although some models assume a uniform weight distribution^{24–26} or anisotropic friction,²⁷ Tanaka *et al.*²⁸ assume each segment is able to vary frictional coefficients independently from segment shape. Since most worm robots do not have variable friction skin, here we assume that anchoring is a result of segment shape, which is coupled to segment length as is common in earthworms and soft robots that mimic them. Interestingly, despite these differences, our results agree with Tanaka *et al.*²⁸ that velocity and energy efficiency have different optimal wave parameters. In our own prior analytical study, rigid centerline models showed the importance of increasing energy efficiency by matching extension and retraction within gait cycles to reduce loss to friction.¹⁶ The unique contribution of this article is that its assumptions are general enough to apply to 50 peristaltic-locomoting robots and to show that softness with respect to gravity dictates a pattern of anchoring that predicts both animal behavior and robot energetic optima.

Based on our prior study,^{16,17,29} we consider an idealized locomoting earthworm model that does not need to slip as it moves and accounts for effects of actuation and deformation, providing a template for understanding peristaltic locomotion with two-dimensional analysis. By employing simplifying assumptions using beam theory, curved plate compression, and volume homogeneity, we demonstrate how worm-like robots can be constructed of any stiffness material with suf-

ficient effective Poisson's ratio and actuation energy density. Furthermore, for a given robot length, either velocity or energy efficiency can be optimized. For a given robot of any size, with a fixed number of segments, moving fewer segments at once not only decreases the cost of transport (COT) but also decreases speed. Although previous robots have been optimized for speed, future robots may need to account for energy costs.^{16,17,22,23} Also, for the first time, this analysis provides an alternative explanation for earthworm observations: perhaps they are balancing speed and COT.

The idealized template analysis we present hereunder is supported by experiments on our robot and on actual earthworms, and by a review of earthworm (referred to as worm throughout the article) robots in the literature. To our knowledge, a dedicated comparative review of earthworm-like robots is lacking, even though worm robots are mentioned in multiple soft robotics reviews.^{30–32} We show that there are many possible design implementations, but that each of them can be characterized by the parameters suggested by this analysis in terms of structure, actuation scheme, and control.

Materials and Methods

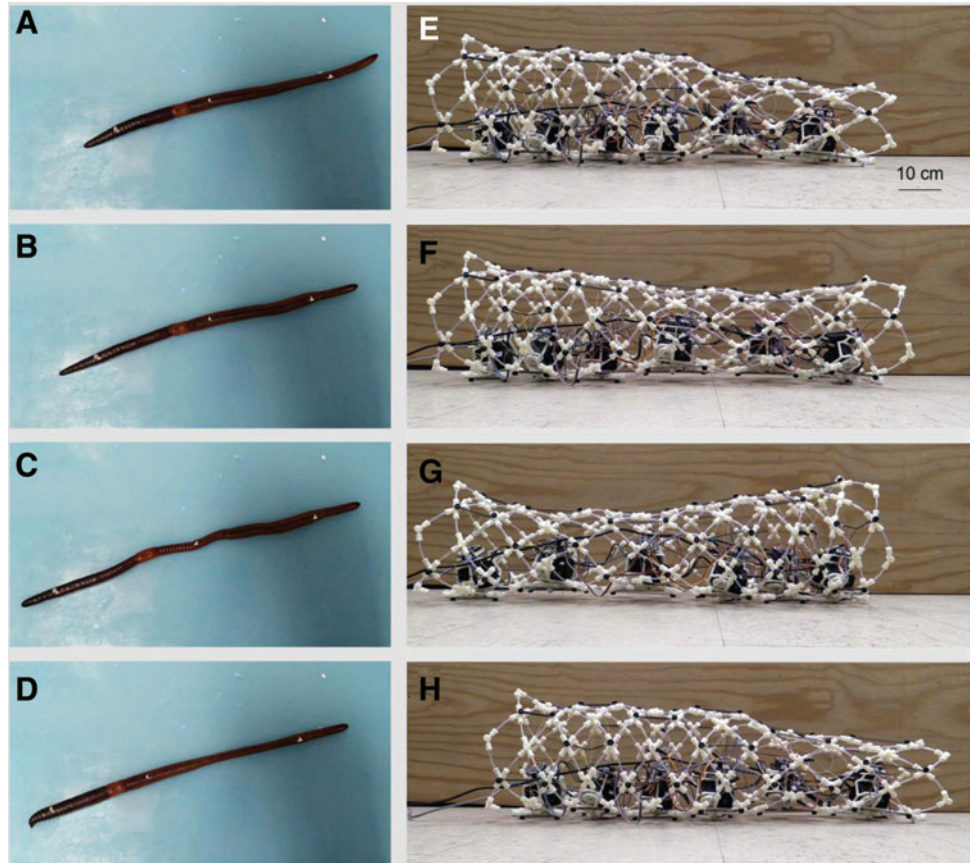
Capturing earthworm data

Large living earthworms (*Lumbricus terrestris*) were ordered from Carolina Biological Supply Company. Multiple videos of earthworm locomotion were recorded from the transverse view using an HD camera (Canon Vixia HF G30, 59.94 fps). From these sets of videos, three videos with three different earthworms (in which the earthworms moved mostly in a straight line) were chosen for counting the number of total segments and number of moving segments during peristaltic locomotion. Sections of the earthworms were marked with nontoxic paint to make counting of segments easier. Tracker video analysis software (Version 4.11.0, Open Source Physics, <https://physlets.org/tracker>) was used to analyze the videos. Anchoring and moving segments were distinguished by visually observing, frame by frame, whether a segment moved or not (Fig. 2A–D). If the position of a segment moved over the span of five frames (0.1 s) we considered the segment to move. At each instant, we calculated the number of moving segments during locomotion. Stills from the videos were extracted to count the total number of segments for each case.

Velocity and COT calculation for Compliant Modular Mesh Worm Robot

Compliant Modular Mesh Worm Robot is a cable-actuated soft robot, composed of nylon tubes and 3-D printed pin-joints.¹⁷ The robot consists of six segments; each segment is actuated using two Dynamixel[®] XL430-W250-T actuators. Cable from each actuator wraps around half the circumference of the segment. As the actuators rotate, cables along the circumference of the segment are uniformly spooled in, thus allowing the mesh-like structure to contract in diameter and extend in length. Linear springs along the length of the segment passively return the segment to its maximum diameter as the cable is spooled out by the actuators. If both actuators rotate at the same speed for the same duration, the segment contracts uniformly. If the actuators rotate at different speeds, the bias in the amount of cable spooled in by the left versus

FIG. 2. (A–D) Sequence of images extracted from a video used to measure number of moving segments and number of anchoring segments during peristaltic locomotion of an earthworm. Markers along the length of the body of the earthworm were used to count number of segments. (E–H) Sequence of images extracted from a video showing straight-line locomotion for our six-segment worm-like robot, Compliant Modular Mesh Worm Robot. Images depict a single wave passing down the length of the body (right to left) allowing the robot to move in the opposite direction to that of the wave. Color images are available online.



right half will allow the robot to turn. In this article, we focus only on straight-line locomotion. The actuators are controlled using an Open CM 9.04 microcontroller that allows programming of the actuators.

The actuators can be programmed to set the sequence in which the segments contract and expand. For this article, we explored the 3×1 , 2×1 , and 2×2 waveforms (as defined in the Results section). The experiments discussed hereunder with CMMWorm were carried out on linoleum tile (coefficient of static friction, $\mu_s = 0.55$) and a DC power supply was used to power the actuators. The actuators were supplied with a constant voltage of 12 V and varying current as required by the actuators. The average electrical power for all three waveforms over five to six waves was measured and at the end the distance travelled in each case was measured (Fig. 2E–H). For the calculation of the average electrical power, the minimum power consumed when the robot is not moving was subtracted from the total power. Velocity of the robot was calculated using the distance travelled divided by the time taken to travel given distance. COT was calculated by dividing the measured average power consumption from the DC power supply by the product of the weight of the robot and velocity of the robot.

Results

Template model: an idealized soft worm with no slip

Earthworms are completely soft with no rigid internal skeleton or exoskeleton. Instead, they maintain their structure with fluid-filled coelom segments that function as a hydro-

static skeleton.²¹ The hydrostatic skeleton provides a constant volume constraint, such that increases in length cause decreases in radius and vice versa. Circumferential and longitudinal muscles change both segment diameter and length. Sequential extension and expansion of the segments along the length result in peristaltic locomotion, in the opposite direction of the wave's travel.³³

An idealized model of an earthworm provides a template (Fig. 3) for understanding peristaltic locomotion in the sagittal plane. Generalized template models that are anchored by more detailed models have been valuable for understanding other types of biologically inspired locomotion.³⁴ This analysis is pertinent to earthworm robots but will not apply to worm-like robots that swim like *Caenorhabditis elegans*,²⁶ locomote using clamping feet, akin to caterpillar crochets,^{1,35} grow like a vine³⁶ or undulate like a salamander.³⁷ Specifically, unlike these examples, we will assume that the body of our idealized earthworm uses only axial extension to move and only radial expansion to contact the ground. Rigid rectilinear locomotion like a snake^{38,39} is similar, but snakes have a skeleton and are relatively rigid, whereas this analysis accounts for soft body deformation (Fig. 3C).

Structurally, we will assume that each segment is a hollow cylinder whose properties can be characterized with properties, including Young's modulus (E), Poisson's ratio (ν), and density (ρ). We will call maximum radius segments "anchoring" segments because they contact the substrate (either flat ground or the interior of a confined space like the inside of a pipe). For simplicity, we assume that each segment is independently actuated with constant rate ($\pm \dot{L}$).

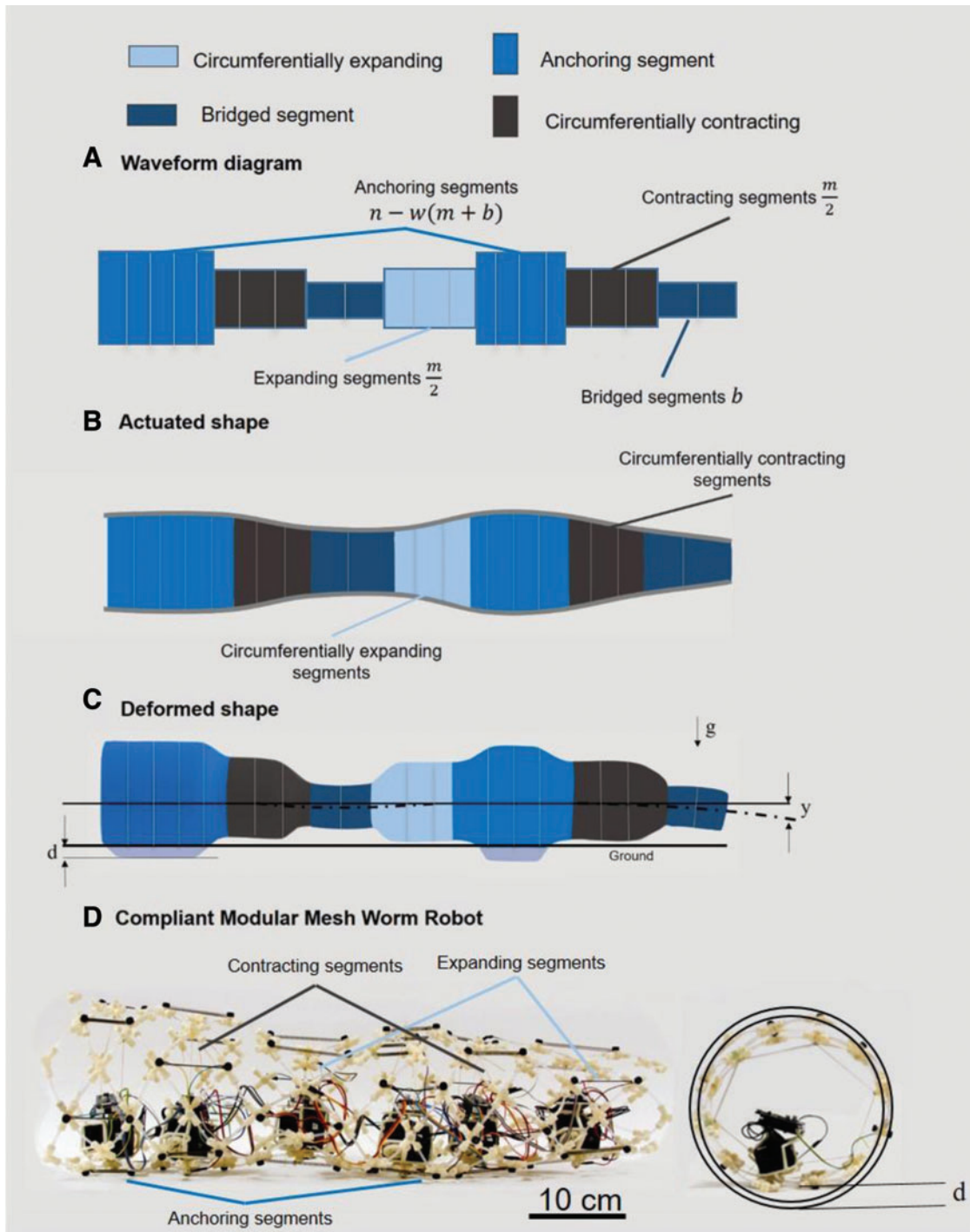


FIG. 3. The waveform is defined by a traveling wave of segments, which can be in any of four states: (1) fully expanded anchoring segment, (2) fully contracted bridged segment, (3) circumferentially expanding, or (4) circumferentially contracting segment. **(A)** Diagram of a multisegment worm robot with two groups of four anchoring segments, separated by eight moving segments. The three contracting segments each increase in length by the constant rate, \dot{L} , and the three expanding segments each decrease in length by $-\dot{L}$, thus, distance between anchor points is constant and anchor points do not slip. **(B)** The actuated shape of the segments will reflect the progress of the contraction and on the real robot some smoothing is observed. **(C)** Finally, soft segments also deform due to gravity. The front cantilever segments bend (y) and the anchoring segments compress (d) due to the weight of the body. **(D)** For example, our worm robot, Compliant Modular Mesh Worm Robot (CMMWorm), is shown during a wave in which four segments are moving (two contracting and two expanding) and two segments are anchoring. The first segment is cantilevered and the anchoring segments undergo compression due to their weight plus the weight of the moving segments. Color images are available online.

The peristaltic wave of an earthworm is defined by the numbers of moving versus anchoring segments and their spatial relationship to each other, which define the waveform shape (Fig. 3B). Assuming accurate control, segments move in waves with pairs of expanding and contracting segments (black and light blue segments in Fig. 3A, respectively) such that anchoring segments need not move relative to the ground.^{14,17} In Figure 3, between active segments (contracting and expanding segments) there are circumferentially contracted inactive (suspended) segments that are referred to as bridged segments.

Eliminating slip is an important constraint, which we have applied to steering and responsive peristalsis,^{29,40} but which is unlike R. McNeill Alexander's prior model. In his seminal 2003 book on the COT of various types of animal locomotion, there is a tacit assumption that an earthworm's weight is uniformly distributed and each segment moves by dragging along the ground. Thus, when a group of segments extend, the body moves forward only if the number of moving segments slides forward more easily than the anchoring segments would slide backward. Thus, the number of segments that can be in motion at any time is limited by the ratio of the coefficient of friction in the backward direction to the summation of coefficients of friction in the backward and forward directions. The setae on the surface of the earthworm could be assisting in inducing anisotropic friction to prevent backward slip. If not, the ratio of moving segments is limited to about 50%.¹⁹ However, we have theorized that peristaltic locomotion can be as efficient as a rolling wheel—where no energy is lost due to slip.¹⁵ In a robot, this can be implemented by lifting segments so that, as they move, they are not in contact with the ground, thereby completely eliminating work done against ground friction (Fig. 3B) as long as extension and retraction have matched rates, that is, the rate of circumferential contraction is equal to the rate of circumferential expansion for a pair of moving segments.¹⁶

Under these assumptions, we will explore the relationships between parameters. We demonstrate how to find the relationship for body speed (v) as a function of actuation rate of a single segment (\dot{L}) and waveform properties (number of waves, w ; number of moving segments per wave, m ; and number of bridged segments, b). We show how both earthworm and robot locomotion can be compared with energy optimal waves and velocity optimal waves.

Calculating velocity

We take the approach of prior publications and calculate expected robot velocity, noting that this will be an upper bound on measured velocity since slip, unintentional turning, and imprecision can decrease velocity. Boxerbaum *et al.*¹⁵ defined velocity of a continuous peristaltic robot as a function of the velocity of the wave as it travels along the length of the body and maximum structural strain. Fang *et al.*²⁵ defined velocity of the robot as a function of the number of moving segments and the rate of stroke of a robot segment, assuming no bridging segments. Fang *et al.* specifies that there should be at least one anchoring segment and that for every circumferentially expanding segment, there should be a circumferentially contracting segment. Thus, the number of moving segments is always even. Seok *et al.*⁴¹ defined velocity for the number of moving segments, $m=1$ or 2, as a

function of length change of each segment, number of waves, and frequency of waves. Horchler *et al.*¹⁷ defined velocity as a function of wave patterns and rate of change of length of a segment, but did not distinguish between bridged segments and moving segments. The actual robot achieves 75% of this predicted velocity.¹⁷

In this study, we define a velocity expression for arbitrary waveform parameters m , b , w , and n . We assume a no-slip condition. Thus, between noncontiguous anchoring segments, there must exist at least one pair of actuating segments (i.e., $m \geq 2$). For simplicity, we will assume that all segments change length at the same rate, $\dot{L} = \Delta L / \Delta T$. Thus, m must always be even. In other words, for every contracting segment there must exist an expanding segment, both actuating at the same rate so that anchoring segments need not slip. The ideal velocity of the robot, v_{ideal} , of a peristaltic robot without slip is directly proportional to the square of the number of moving segments, m (Appendix I), and the number of waves, w , traveling within the robot, and the rate of change of length of a segment, \dot{L} .

$$v_{\text{ideal}} = \frac{wm(m+2b)}{4n} \dot{L}, \quad (1)$$

where b is the total number of bridged segments between a pair of moving segments within one wave and n is the total number of segments in the robot.

The ideal velocity equation shows that a high velocity can be achieved with more moving segments (m), thus reducing the number of anchoring segments ($n - (m + b)$). However, all the segments cannot be moving at once because then the robot would rely on isotropic friction (and might not be able to extricate itself by moving backward). A key constraint we use is that not more than half of the segments can be moving in a single wave (or else the robot would tip on flat ground when the wave begins). However, even if tipping does not occur, soft deformation can limit the number of moving segments.

Limiting effects of soft segment deformation

Softness is an essential advantage of worm robots, but segment compliance can adversely affect movement. Specifically, in this section we look at how compliance affects the robot's ability to lift segments off the ground, which is important for preventing work against friction through slip.^{15–17} In order for moving segments to rise off the ground, the change in radius (ΔR) due to actuation must be larger than vertical deformations of the centerline.

We consider two types of vertical deformations (Fig. 3C). First, there is the effect of the bending of the unsupported segments, y . This is largest at the anterior and posterior of the robot when the whole wave ($m + b$ segments) is cantilevered from the body. The second type of deformation in the vertical direction comes from compression of the anchoring segments, d , as they support the weight of the body, including segments that are off the ground. It is this second effect that turns out to be most important for worm robots with fewer segments. Combining these two, we can state

$$|\Delta R| > y + d. \quad (2)$$

To use simplified beam theory to approximate these deformations, we make some key assumptions. First, the segments are modeled as thin cylindrical shells. Second, all segments are assumed to have the same mass. Third, each segment has uniform anisotropic Young's modulus, that is, Young's modulus E_c for circumferential deformation is not equal to Young's modulus E_l for longitudinal deformation. We approximate the cantilevered front segments as a cantilever beam under a uniform load due to segment weight to determine the deformation y . The beam bending between two anchors is much less than this amount because those segments are supported at both ends.

Furthermore, for the case of small deformations, ΔR can be approximated as

$$|\Delta R| \approx \vartheta R \frac{\Delta l}{L}, \quad (3)$$

where ϑ is Poisson's ratio, R is radius, Δl is change in segment length, and L is segment length. Substituting into Equation (3) the constraint defined in Equation (2) yields [Appendix II shows the substitutions and the cancellations to derive Eq. (4)]:

$$\vartheta \frac{R}{L} \Delta l > \frac{(m+b)^4 m_{\text{seg}} g L^3}{8E\pi R^3 t} + \frac{m_{\text{seg}} g n}{(n-w(m+b))} \frac{(R)^3}{2E(Lt^3)}, \quad (4)$$

where m is the number of segments in a single wave, b is the number of segments bridged between a pair of moving segments, m_{seg} is the mass of a single segment, g is acceleration due to gravity, E is Young's modulus, R is the radius of the segment, t is the thickness of the segment, and w is the total number of waves traveling down the length of the robot.

COT as a function of waveform, geometrical properties, and Poisson's ratio

A common metric to characterize actuators is how much power is output normalized by weight.¹⁶ In this study, we neglect kinetic energy because most worm robots are relatively slow and we neglect frictional losses because we are assuming perfect control eliminates slip. Thus, we can approximate the required power output by determining the strain energy. If the primary energy cost is directly proportional to the change in length, assuming the structure to have linear elasticity, strain energy is

$$U = \frac{1}{2} V E_l \varepsilon^2, \quad (5)$$

where V is the volume of the segment, E_l is its Young's modulus in the longitudinal direction, and ε is the strain in the deformed segment. The actuators must exert at least this much energy (plus more to overcome mechanical inefficiencies). We are assuming that this energy is not recovered when the structure is released based on our experience with worm robots. Thus, normalizing by time and segment weight, the power to weight ratio will be limited by

$$P > \frac{V E_l \varepsilon^2}{2 m_{\text{seg}} g \Delta T}, \quad (6)$$

where m_{seg} is segment mass, ΔT is change in time, g is the acceleration of gravity, and P is the power to weight ratio. Assuming a segment has uniform density, we substitute

Equation (6) into (4), which determines how much segments have to move to lift off the ground. After simplifying (Appendix II), we obtain

$$COT = \frac{P}{v_{\text{ideal}}} > \underbrace{\frac{1}{\vartheta} \frac{E_l}{E_c} \left[\frac{n(m+b)^4}{2wm(m+2b)} \left(\frac{R}{L} \right)^{-3} \right]}_{\text{Bending Cost of Transport Factor}} + \underbrace{\frac{2\pi n^2}{wm(m+2b)(n-w(m+b))} \left(\frac{R}{L} \right) \left(\frac{R}{t} \right)^2}_{\text{Compression Cost of Transport Factor}}. \quad (7)$$

The ratio of power to velocity and weight is P/v_{ideal} , since P is defined as power to weight ratio in Equation (6); in turn, this is equal to the COT, a common dimensionless metric in robots, which is defined by the energy expenditure per unit weight per distance traveled. Thus, Equation (7) shows how the power requirements of peristaltic locomotion are fundamentally limited by desired speed (v_{ideal}) as well as the geometry and material properties of the segments (characterized by ϑ , R , L , t , and $\frac{E_l}{E_c}$), the actuation (which will determine E_l and L) and the waveform (which is characterized by n , m , b , and w). Even though geometrical properties (R , L , and t) are important parameters for energy optimization, it is the ratio of segment radius to segment length (R/L) and ratio of segment radius to segment thickness (R/t) that is used to optimize COT. In addition, calculation of the velocity of the robot includes the rate of change of length and, thus, COT depends on the rate of change of length and geometric ratios. We discuss how these parameters relate to existing robots in the following sections.

Structural implications of analysis: how current worm-like robots couple length and diameter

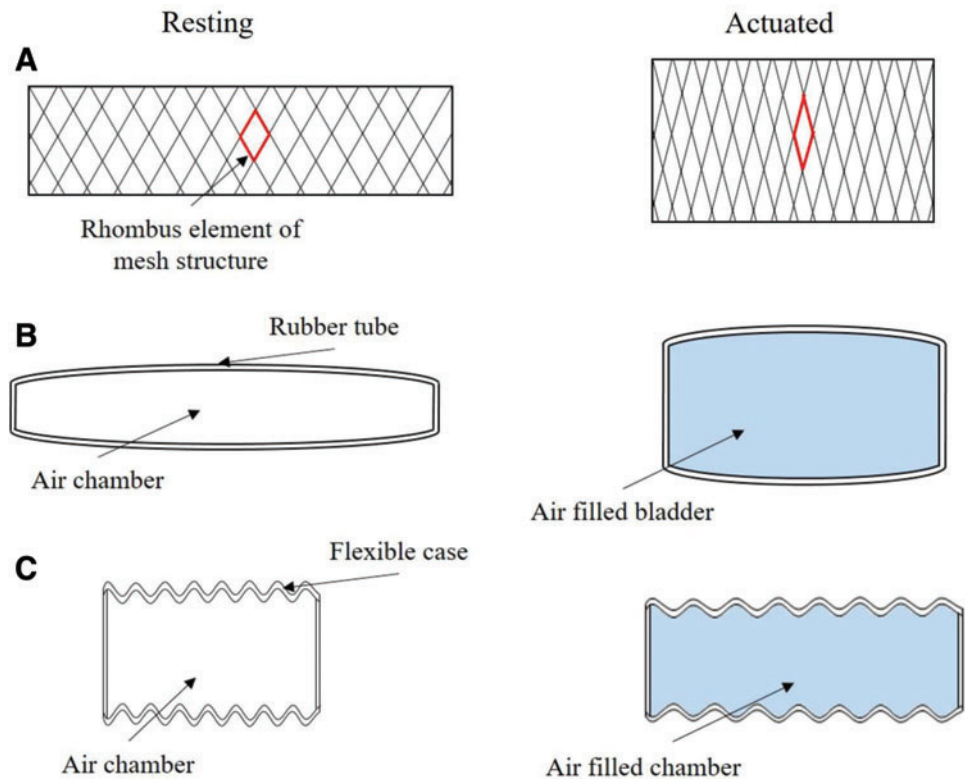
This analysis [especially Eqs. (4) and (7)] show the importance of maximizing Poisson's ratio, ϑ . If the constraint of Equation (4) is not met, the robot will have to slip along the ground unless some other way of actuating anchoring is used, potentially doubling the number of actuators on the robot. If the constraint of Equation (7) is not met, the robot will not have sufficient power to deform itself at the desired rate.

Although earthworms have circumferential and longitudinal muscles, earthworm-inspired robots often use only one actuation method, that is, circumferential or longitudinal actuation, rather than using both. This is made possible by length-diameter coupling, but a robot's coupling mechanism need not use incompressible liquid in a constant volume system, as in an earthworm. The critical challenge is achieving a large effective Poisson's ratio, ϑ which characterizes how length and diameter are coupled:

$$\vartheta \approx \left| \frac{\Delta R/R}{\Delta L/L} \right|. \quad (8)$$

Researchers in the past four decades have developed multiple ways of achieving length-diameter coupling and corresponding Poisson's ratio that allow structures to locomote using peristalsis. For example, soft mesh structures have often been used to achieve this effect. The basic element

FIG. 4. The body structure enables segments to change length horizontally, while often changing in diameter (vertically) as well. Three of the most common segment structures are shown in their rest and actuated states. (A) Mesh structures rely on rhombuses with constant side length, and can be actuated using servomotors, shape memory alloys, or other actuation schemes. (B) PAMs lengthen when the pneumatic bladder is pressurized using air. PAMs are either used in pairs or require a passive mechanism, like springs (not shown in the figure) to return to their natural state when the bladder is depressurized. (C) Bellows structures are capable of large axial strain but small circumferential strain. The bellows are made of flexible materials such as rubber or silicone and extend longitudinally when actuated. PAMs, pneumatic artificial muscles. Color images are available online.



of a mesh structure is a rhombus, in which a change in width causes a change in the length (Fig. 4A). Mesh structures can be made of expandable nylon as is done in MeshWorm⁴¹ or using 3D printed pieces and flexible tubes to construct a mesh structure as is done in CMMWorm.¹⁷ McKibben artificial muscles^{8,41} consist of an expandable bladder inside a tubular mesh made of relatively inelastic fibers. When the bladder is inflated, the diameter of the mesh increases (Fig. 4B). This converts circumferential pressure forces into an axial contraction force. Springs are generally used to provide a return force as the bladder is deflated.⁸ Bellows can achieve high axial strain and hence are used in multiple peristaltic robots (Fig. 4C).^{13,42–49} Although the length-diameter coupling is low in bellows structures, due to the scalability and simple actuation techniques, these structures have been commonly used, especially as the middle segment in two-anchor worm robots, which are discussed as follows.

It is important to note that ν in Equation (7) is the effective Poisson's ratio of the entire structure. Thus, although a material's Poisson's ratio is limited to range between -0.5 and 0.5 , metamaterials and structural linkages can have higher effective Poisson's ratios. For example, the effective Poisson's ratio for our mesh robot, CMMWorm is 1.4 .¹⁷ Using the simplified aforementioned equation, the approximate Poisson's ratio for PEW-RO⁵⁰ is 2.9 and for Meshworm⁴¹ is 4 . In many origami and kirigami structures, positive or negative Poisson's ratios can be designed.⁵¹ Note that when Poisson's ratio is negative, the structure is auxetic,⁵² and in that case the waves travel in the same direction as the body travels.⁵¹

Implication of analysis for actuation: artificial muscles for fast, compact, and precise movements

Actuation choices are critical for peristaltic robots, which are known for their large number of kinematically redundant degrees of freedom.⁵³ The aforementioned analysis suggests three key characteristics for actuators that determine the performance of a worm-like robot. First, high speed, and thus high strain rate (\dot{L}) will maximize velocity [Eq. (1)]. Second, compact actuators with high power to weight ratio (P) maximize efficiency [Eq. (7)]. Third, this analysis assumes that each segment moves precisely to avoid slip, minimizing frictional losses. However, the analysis also shows that any actuator stiffness can be appropriate (Fig. 5), especially if the surrounding structure provides anisotropy in the form of additional circumferential stiffness E_l/E_c .¹⁴

Typically, if segment stiffness is sufficient, the actuators need only pull one way and the passive compliance of the structure acts as a return spring. Turning¹⁴ or climbing⁵⁴ requires additional actuators. Reduced actuation as in^{15,55,56} can enable peristaltic locomotion with a single actuator for the whole robot. However, in such cases, the robot is less modular and cannot adapt its gait as needed.

Traditional actuators can be used, but can be heavy and difficult to integrate with a compliant segment structure. For example, servomotors can tighten cables around the diameter or zig-zagged along the length.¹⁷ These are easy to control, have a high energy density and a rapid response time. However, they are typically heavy blocks that interrupt the smooth body structure and cause limitations in structural

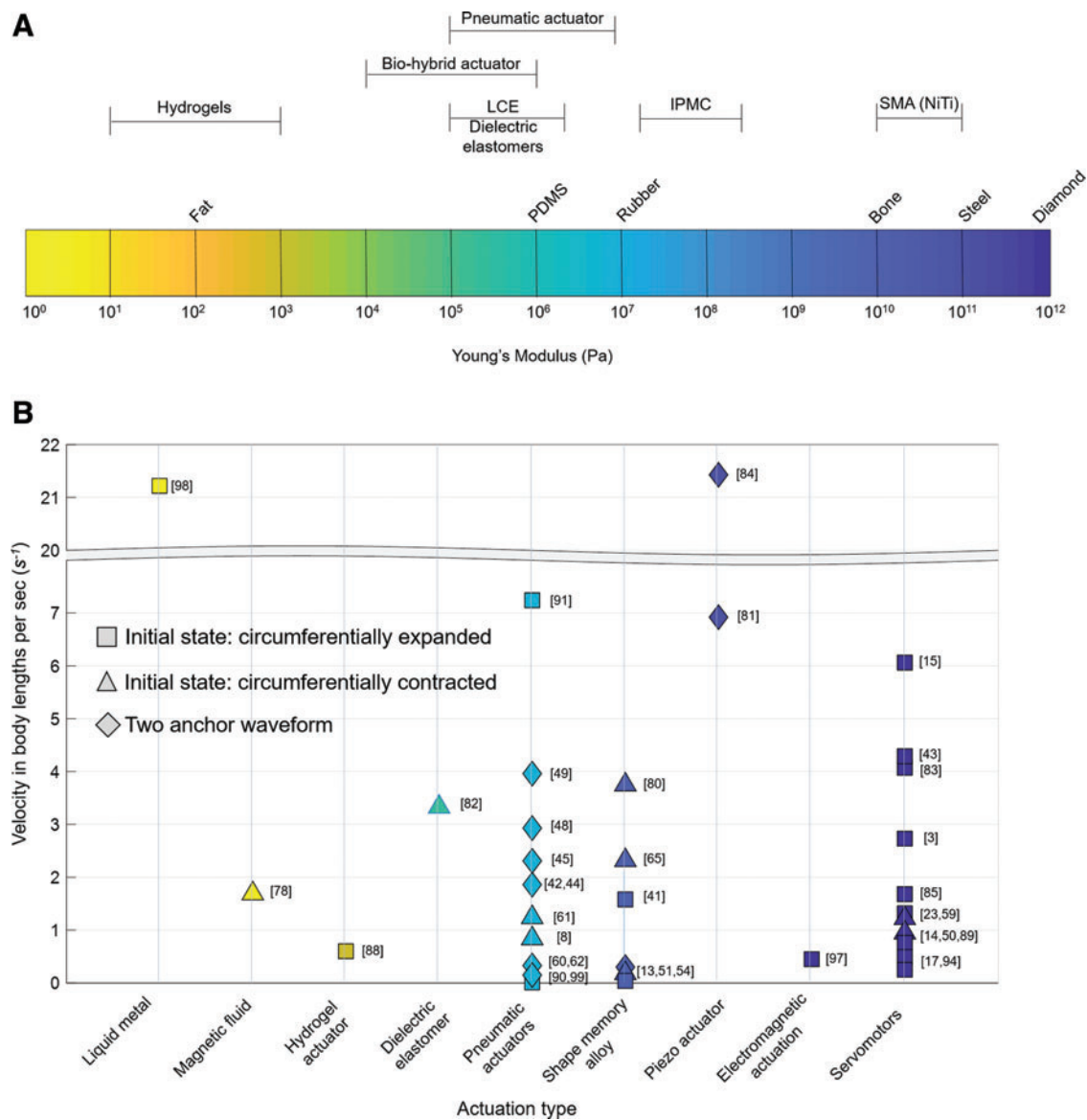


FIG. 5. Peristaltic devices have been described with many different actuators. **(A)** Each actuator type consists of material with a characteristic Young's modulus. **(B)** The most popular actuation schemes are pneumatic actuators, shape memory alloys, and servomotors. Robot speed normalized by body lengths is not correlated with body stiffness—there are fast robots for stiff piezoelectric actuators and for liquid metal actuators. The colors in **(B)** correspond to the Young's modulus as shown in **(A)**. *Triangle, square, and rhombus symbols* differentiate the type of waveform the robot uses for locomotion. Note the break in the *Y* axis between 7 and 20. Numbers in *brackets* refer to references in the bibliography. Color images are available online.

compliance and geometrical limits. Pneumatic pressure can be used to change segment shapes,^{8,44,49,57–62} but require compressors. On-board compressors are typically rigid and compressing gas is an inefficient process. Wehner *et al.*⁶³ compare pneumatic energy sources for soft robotic applications and provide a framework to support the design of untethered pneumatic soft robots. Pneumatic systems, however, are less resistant to punctures and high temperatures. Pneumatic robots that incorporate McKibben actuators are considered hyperelastic structures.⁶⁴ The analysis presented in this article does not account for the nonlinearity of those actuators, preferring to focus on a more general approach, but these nonlinearities could be incorporated in future study.

Thus, worm robots are often some of the first body designs to test new soft actuators. Shape memory alloys (SMA) are soft and light, and are, therefore, common in worm robots and worm robot skins.^{13,41,54,65} A major advantage highlighted by Seok's SMA controlled worm is that the entire soft body is resilient to damage such as being stepped on or hit with a hammer.⁴¹ When heated, SMA can decrease diameter⁴¹ or length,⁵⁴ and the segment returns to its original shape when cooled. This can be slow. Furthermore, in our experience, it can be challenging to precisely pair heating and cooling rates.

Developing novel soft actuators that can replace their metallic counterparts is of broad interest.^{66–68} The use of polymers and other softer actuators, such as hydrogels and

bio-hybrid actuators for worm robots, has seen remarkable growth in the last few years.^{67,69–76} These actuators might be able to avoid the problems with heat actuation by responding to light, chemical concentration or electrical current.⁷⁷ A major drawback of these soft actuators is their inability to produce large force, which means the structure of the body has to be correspondingly soft. However, soft actuators promise to improve in terms of speed, reliability, power consumption, robustness, and ability to be easily integrated within the structure.

Implications of analysis for waveform control: effective gait patterns for locomotion

The shape of the peristaltic waveform can be altered for speed [Eq. (1)] or efficiency [Eq. (7)]. Each segment can be in one of the four possible states: circumferentially expanded (anchoring), circumferentially contracted (bridging), expanding in diameter, or contracting in diameter (Fig. 3). We call the spatial pattern of these states the “waveform.” Just as a legged robot might have many possible gaits depending on the number of legs, a worm-like robot can be controlled with different waveforms depending on the total number of segments in the structure (n). We define each gait by the number of moving segments per wave (m), number of waves traveling down the length of the body (w), and number of bridging segments between expanding and contracting segments (b). The waveform determines the speed and efficiency of peristaltic devices.

In the literature, there are several different categorizations of waveforms for worm-like robots.^{17,62,69} The resting or initial state can be circumferentially contracted (Fig. 6AII, II) or expanded (Fig. 6AIII, IV). In either case, the segments can be controlled with a complete transition or with traveling waves, depending whether a new wave starts before the previous one finishes. In the case of traveling waves, the number of moving segments is constant if there are enough segments to fit the entire pattern. Figure 6AIV is most similar to our robot, CMMWorm, and is the type of robot for which we will consider optimization.

However, there are many robots that use a two-anchor waveform (Fig. 6B) in which the middle segment is never designed to anchor. This allows independent design for anchoring segments and expanding segments. Instead of having a wave of radial contraction travel down the length of the body, the robot locomotes by discretely expanding and contracting in diameter, and extending and retracting in length. Segments capable of circumferential strain are capable of anchoring, whereas the segments capable of longitudinal strain are used for forward motion. The minimum number of segments required for this type of locomotion is three, and additional pairs of segments can be added.

Velocity-optimal and COT-optimal waves

What is the best waveform shape for a particular robot? This analysis allows us to supplement empirical results with theoretical optima for either speed or COT. Note that because we made many simplifying assumptions (no slip, segments are uniform thin hollow cylinders, small deformations, and perfectly controllable segments), the relative contributions of bending versus compression versus other types of energy

expenditure might be different for specific designs. However, the general optimal waveforms should be preserved even if precise deformation calculations vary.

First, consider a short ($n=6$) worm robot similar to our robot CMMWorm. There are three possible gaits that meet the aforementioned constraints (shown in Table 1). We previously called these 2×1 , 2×2 , and 3×1 ,¹⁷ where the first number represents the total number of moving segments per wave ($m+b$) and the second is the number of waves along the body (w). For $n=6$, in all cases $m=2$, but there may either be one wave with a bridge segment (3×1 , $w=1$, $b=1$), or one or two waves without a bridge segment (2×1 or 2×2 , $w=1$ or 2 , $b=0$). Previously, we showed that the 3×1 and the 2×2 waves were expected to be equally fast. In this study, we extract geometrical and structural properties from our robot CMMWorm, where the ratio of radius to length of segment, $R/L=0.5$, ratio of radius to thickness of segment, $R/t=30$ and the Poisson’s ratio=1.4. In addition, CMMWorm has an anisotropic Young’s modulus, that is, the effective Young’s modulus in the longitudinal direction is not the same as that in the circumferential direction; the actual ratio is $E_c/E_l=3 \times 10^4$. Inserting these numbers into inequality (7), we calculated the robot’s COT for these three different waveforms. Next, we empirically measured the COT for the same waveforms in our robot as described in the Materials and Methods section and compared it with our calculated COT. These results are shown in Table 1. Our analysis correctly predicts that the 3×1 wave is more energetically efficient, followed by the 2×2 wave, followed closely by the 2×1 wave. Furthermore, due to the modularity of our robot, we removed two segments and performed a 2×1 wave on a four segment robot. The measured COT for this case was 73.6, which as predicted by our analysis is greater than a six-segment 3×1 waveform.

It is not surprising that the measured COT is much higher than the theoretical minimum predictions. The power calculated is the mechanical power required to deform the structure based on mechanics calculations. However, the power measured is the electrical power input to the motors. Electrical power was chosen because it is both easier to compare across different actuation types, and more relevant to battery power usage for future untethered robots. Therefore, the measured COT will be higher because it includes frictional and inertial losses in the motors and transmissions, cable friction, ground-mesh interactions,¹⁷ and electronics. The losses in converting electrical to mechanical energy is often substantial. For reference, Dynamixel’s actuator documentation (<http://emanual.robotis.com/docs/en/dxl/x/xl430-w250/>) suggests a maximum expected efficiency of 25% and this efficiency decreases for variable speeds and higher torques. This value would be multiplied by another efficiency factor that represents losses when converting actuator power to structural deformation of the 3D printed mesh structure. Thus, we expected the measured COT to be greater than an order of magnitude more than the predicted minimum COT. However, the relative magnitudes across different waveform shapes show the same pattern, indicating that the analysis correctly predicts which waveforms are energetically optimal. It may be possible to further decrease COT by optimizing ΔL for different waveforms [Eq. (4)], or changing other parameters in Equation (7), or redesigning the actuation system to increase electrical-to-mechanical efficiency.

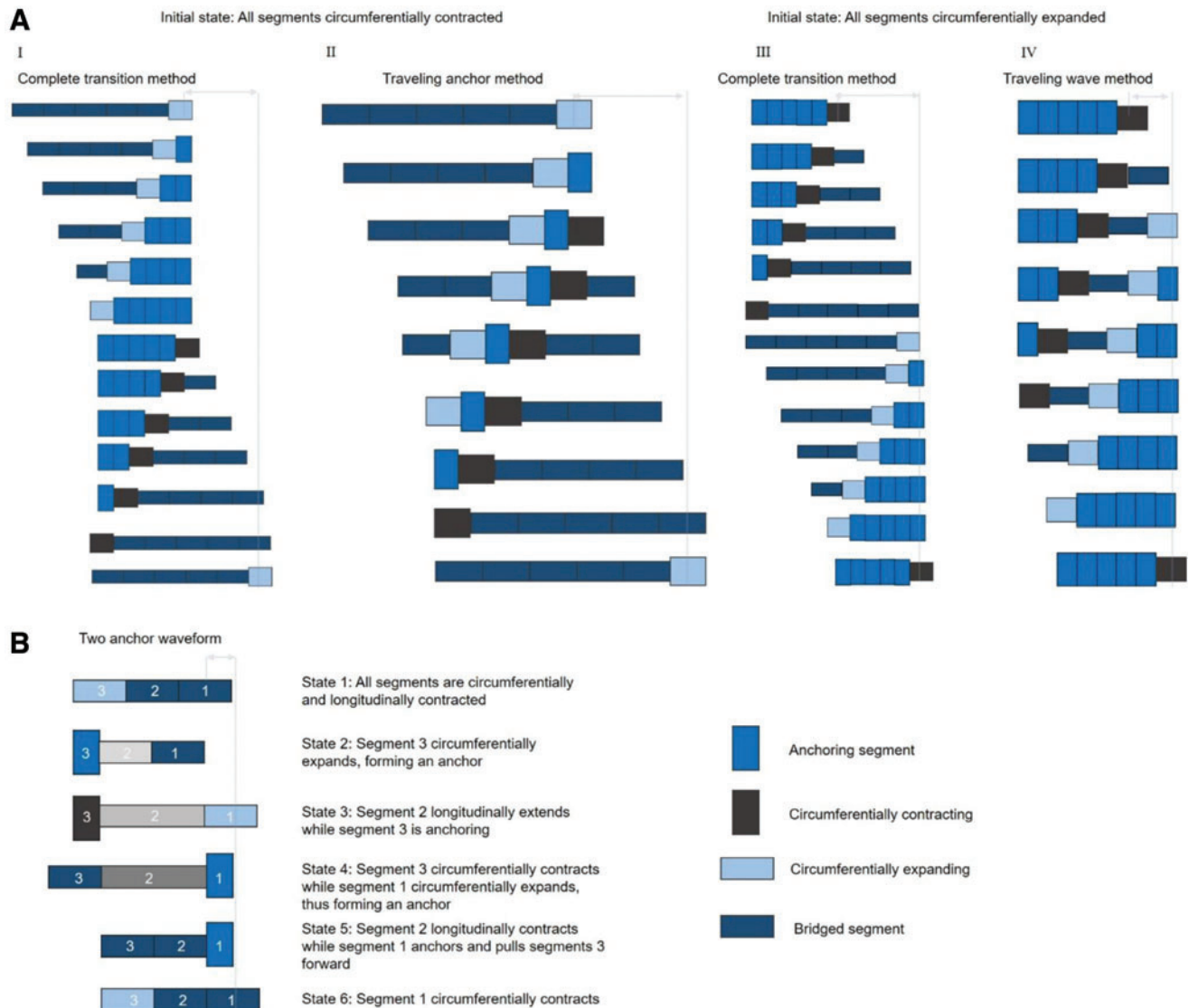


FIG. 6. There are different types of waveforms commonly used in peristaltic devices. (A) If there are large number of segments (in this case shown with six, and with positive Poisson's ratio), the original resting state can be either circumferentially contracted (I, II) or expanded (III, IV). In both cases, either all segments can actuate before any segments return to resting state (I, III) or a traveling anchor can be generated with a constant number of anchoring segments (II, shown with one anchoring segment, and IV, shown with four anchoring segments). (B) Two-anchor waveforms have three segments but the *middle* and *end* segments have different functions, and thus a coupling ratio is not required. The *middle* only extends in length, and needs never anchor. The ends need only anchor and release (not extend). Color images are available online.

Next, we show that a difference in speed optimal (Fig. 7A) and energy optimal (Fig. 7B) gaits persists in longer worm robots by considering all possible waveforms for $n = 100$. In this case, the number of moving segments can vary between 2 and 50 for a single wave. The maximum no-slip velocity occurs with 2 waves with 49 segments moving (case c: 24 pairs of actuating segments and 1 bridged segment, which leaves only 2 anchoring segments) when the velocity would be 12 times the segment strain rate. However, the COT of such a wave is 71.9, which is relatively high. The most efficient waveform would have 10 waves with 6 moving segments in each wave (case a). This waveform has only 60% of the segments moving, and thus a speed approximately equal

to the segment strain rate. However, the actuators would only need to overcome the segment stiffness required to keep fewer segments aloft. Between these two waveforms is case b in Figure 7, which is an approximation of the waveform of an earthworm. Earthworms move $\sim 48\%$ of their segments (according to our observations) with one or two waves traveling down the length of the body. For a 100 segments worm, that would correspond to 2 waves of 24 moving segments.

To generalize for arbitrary numbers of segments, we perform this energy optimization for each worm length from $n = 4$ (the minimum) to 150. In Figure 8A, the optimal power requirements are dominated by compression cost at low segment numbers, but the bending cost increases for higher

TABLE 1. WAVE PROPERTIES AND CORRESPONDING IDEAL VELOCITY AND COST OF TRANSPORT FOR THE DIFFERENT WAVEFORMS FOR A SIX-SEGMENT ROBOT

			
Total No. of segments (n)	6	6	6
Actuating segments per wave (m)	2	2	2
Bridged segments (b)	0	1	0
No. of waves (w)	1	1	2
Anchoring segments	4	3	2
Ideal velocity normalized by \dot{L}	$0.166 \dot{L}$	$0.33 \dot{L}$	$0.33 \dot{L}$
Calculated ideal velocity (cm/s)	0.55	1.1	1.1
Measured velocity (cm/s)	0.36	0.79	0.77
Bending COT factor	0.015	0.04	0.007
Compression COT factor	1.72	1.14	1.72
Total predicted minimum required COT	1.735	1.18	1.727
Measured COT ^a	67.7	30.8	59.7

Italic values indicate rate of change of length.

A still from the waveform is shown in the first row and below that wave properties and bending and compression COT factors. \dot{L} for CMMWorm is 3.33 cm/s.

^aAverage electrical power input to the robot divided by velocity, which one expects to be much higher than rate of work done. COT, cost of transport.

Color images are available online.

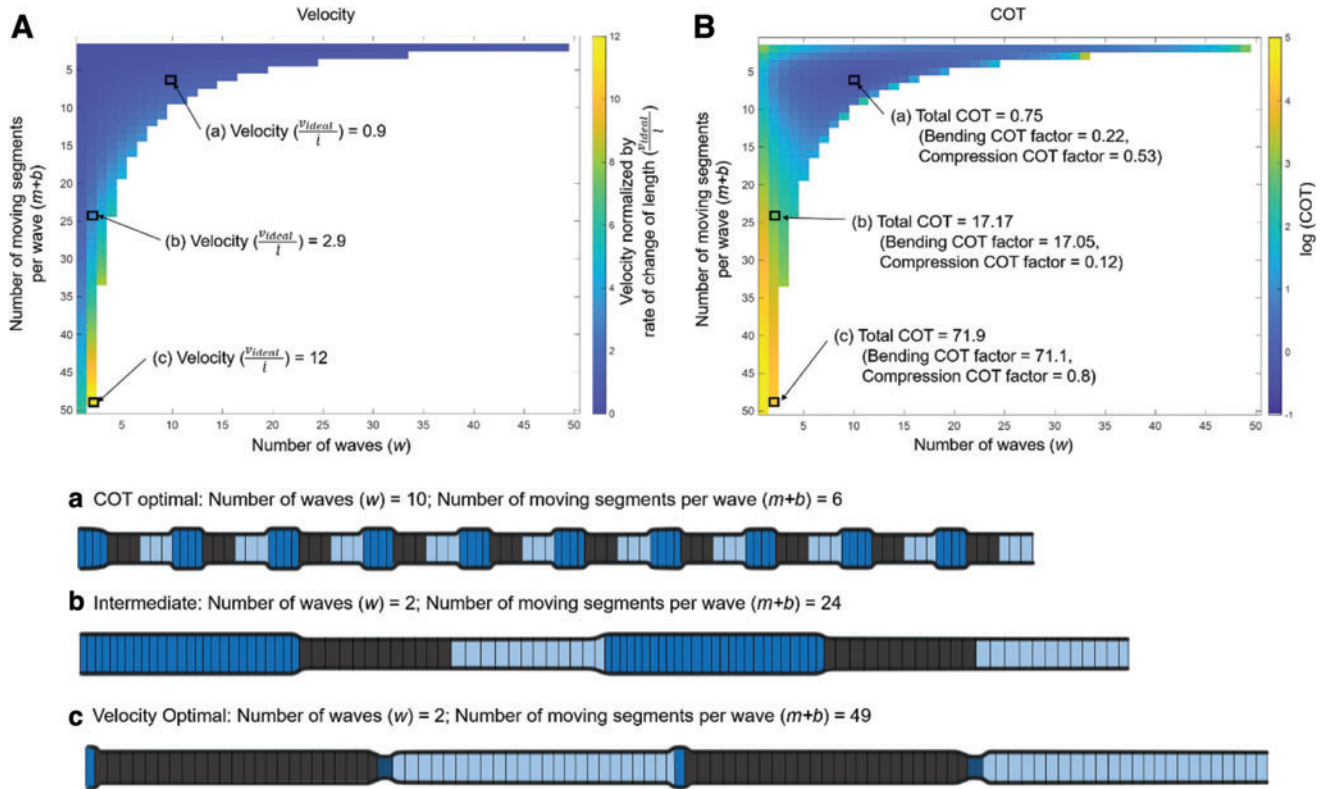


FIG. 7. For a given number of segments, in this case 100, we calculate the velocity (A) and COT (B) for all possible waveform combinations. The waveform using the least COT and the waveform with the maximum velocity are highlighted by a black box (case a and case c, respectively). For minimum COT, the waveform is 10 waves of 6 moving segments each wave. The ratio of moving segments to anchoring segments is 1.5. In contrast, for maximum velocity, the waveform is 2 waves of 49 moving segments each wave. The ratio of moving to anchoring segments is 49. From our observations, earthworms move approximately half their segments using one or two waves (case b). Here there are 2 waves of 24 moving segments each wave. The ratio of moving to anchoring segments is 0.92. Color images are available online.

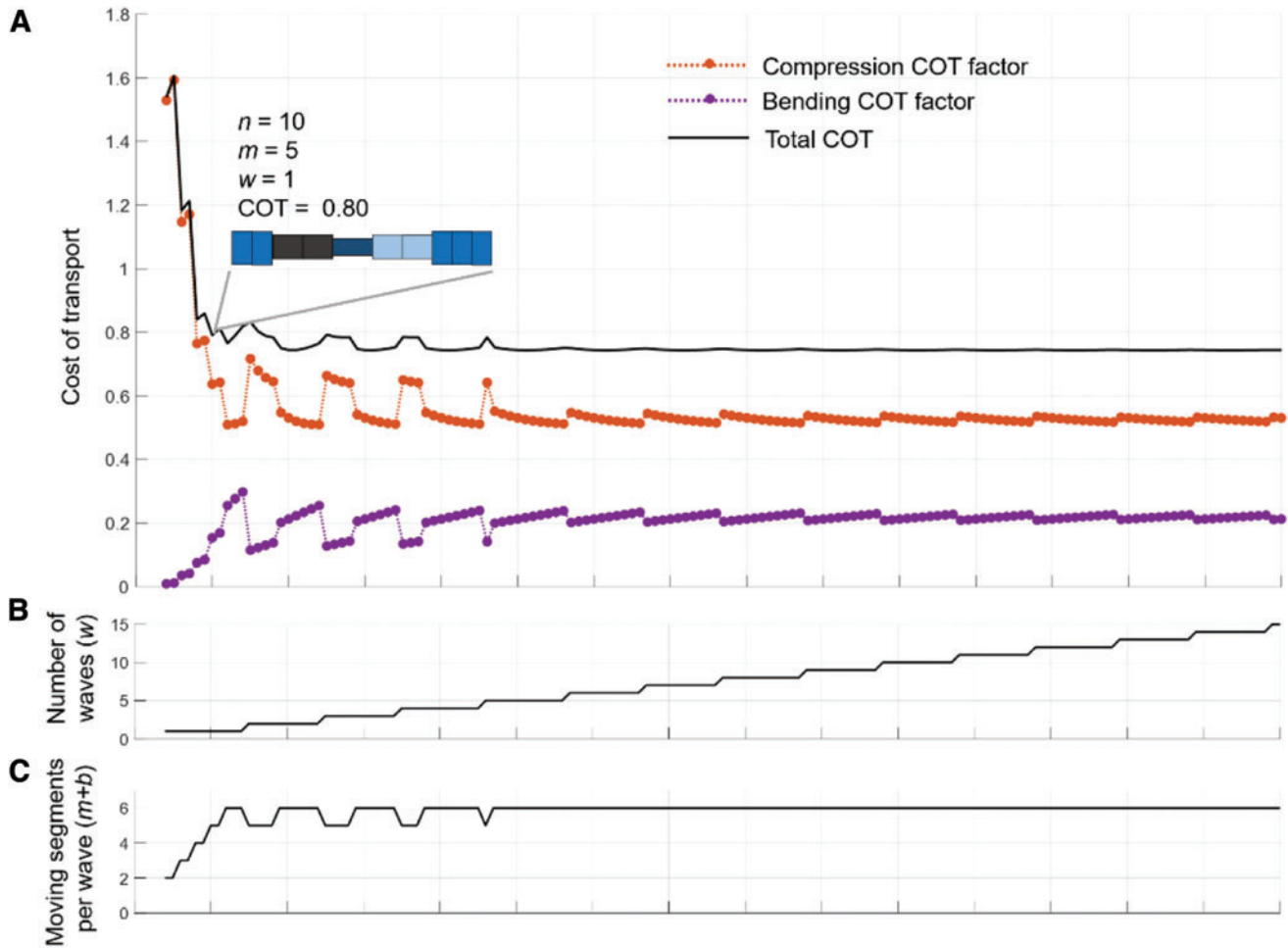


FIG. 8. Waveform parameters corresponding to the minimum COT (**A**) The best COT for a peristaltic robot decreases as the number of segments increase until leveling off at ~ 0.8 after 10 segments. *Orange line* shows compression COT factor and *purple* shows bending COT factor. The summation of both these factors is the total COT (*black line*). Bending COT is always smaller than compression COT since the number of segments that are being cantilevered at the beginning of the wave are always few. (**B, C**) The waveform parameters that result in best COT above are shown. As the number of segments increases, it is suggested that the number of moving segments be limited and the number of waves increase, allowing small cantilevers with large numbers of moving segments. The maximum number of moving segments is 6 in a single wave, which is constant beyond 48 segments; however, the number of waves continues to increase from 5 to 15. (**D**) Thus, the percentage of moving segments for energy-optimized waveforms (*black line*) is much lower than for velocity optimized waveforms (*blue line*), especially as the number of segments increases. We show our robot (CMMWorm) velocity and energy optimal data for four and six segments. We also show percentage of moving segments for earthworms in this case, where we took measurements from three different worms with total number of segments (n)=142, 147, and 144. The number of moving segments for each case was $m + b = 70, 67,$ and 64 , respectively. (**E**) Ideal velocity for velocity optimal waveform (*blue line*) ranges between $0.2L$ to $18L$ and goes off the scale as the number of segments increases beyond 20, whereas for the COT-optimal waveform (*black line*) the velocity stops increasing just under L . COT, cost of transport. Color images are available online.

numbers. The optimal total COT is high when the number of total segments is low; as the number of segments increases, the COT decreases and is almost constant as the number of segments increases beyond 10. The optimal 10 segment worm waveform is shown: It has one wave that travels down the body with 5 moving segments (1 bridge, 2 expanding and 2 contracting). The other five segments are stationary anchoring segments.

The specific gait pattern corresponding to the minimum COT for each robot length is shown in Figure 8B and C. With <12 segments, the energetic optimal waveform is 1 wave with

the size of the wave increasing (more moving segments per wave). For robots with more segments, additional waves should be added, with about five or six segments moving in each wave. (Note that when the number of moving segments is odd, a bridge is needed, $b=1$; otherwise, when the number of moving segments is even, $b=0$).

Thus, we can compare the percentage of moving segments for waveforms optimized based on velocity [Eq. (1)] and COT (Eq. (7)) in Figure 8D. As the number of segments increases beyond 12, the percentage of moving segments for velocity optimization is between 90% and 98%, whereas for

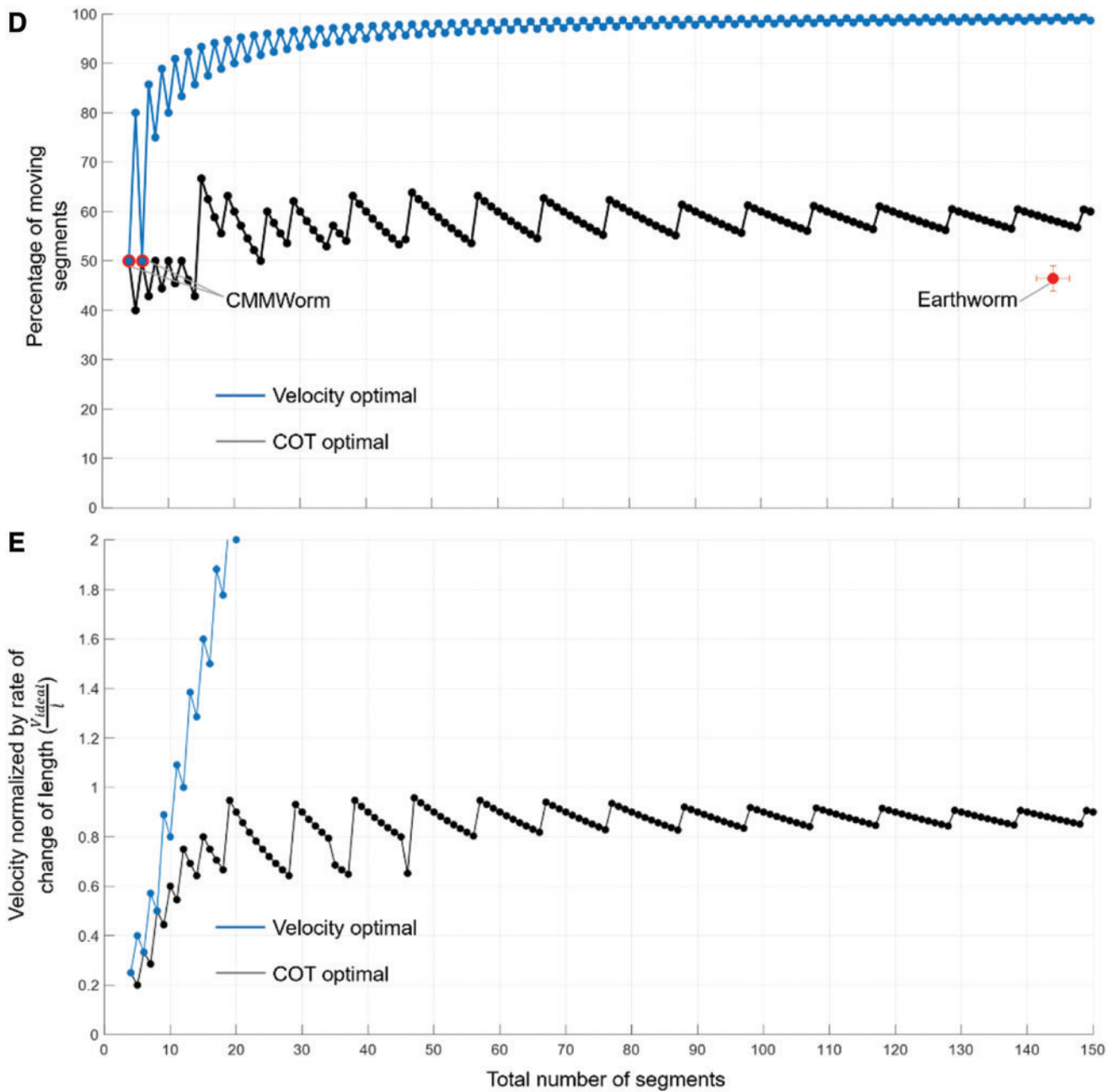


FIG. 8. (Continued).

energy optimization the percentage is between 50% and 70%. This suggests an explanation for why earthworms (red dot) have so many anchoring segments—the faster waveforms require much more energy. Results from CMMWorm (red circles) are consistent with predictions of the equations.

As the total number of segments increases, the ratio becomes greater than one; that is, the number of moving segments is greater than the number of anchoring segments. Figure 8E emphasizes the velocity for *energy*-optimized waveforms, although velocity for energy-optimized waveforms is less than *velocity* optimized waveforms (energy-optimized velocity ranges between 0.2 – $1.0 \times$ segment strain

rate as compared with 0.2 – $18 \times$ segment strain rate), the *COT* for the energy-optimized waveforms is much lower (COT for energy-optimized waveforms is <1 and COT for velocity optimized waveforms can reach 250).

In Figure 9, we compare ideal velocity as a function of number of moving segments, optimal COT and waveforms for published peristaltic robots. It seems likely that most of these robots are designed for maximum speed, since peristalsis can be a slow form of locomotion. As described earlier, for fewer numbers of segments, higher velocity is achieved when there are more moving segments; however, this might not be the most energy efficient waveform.

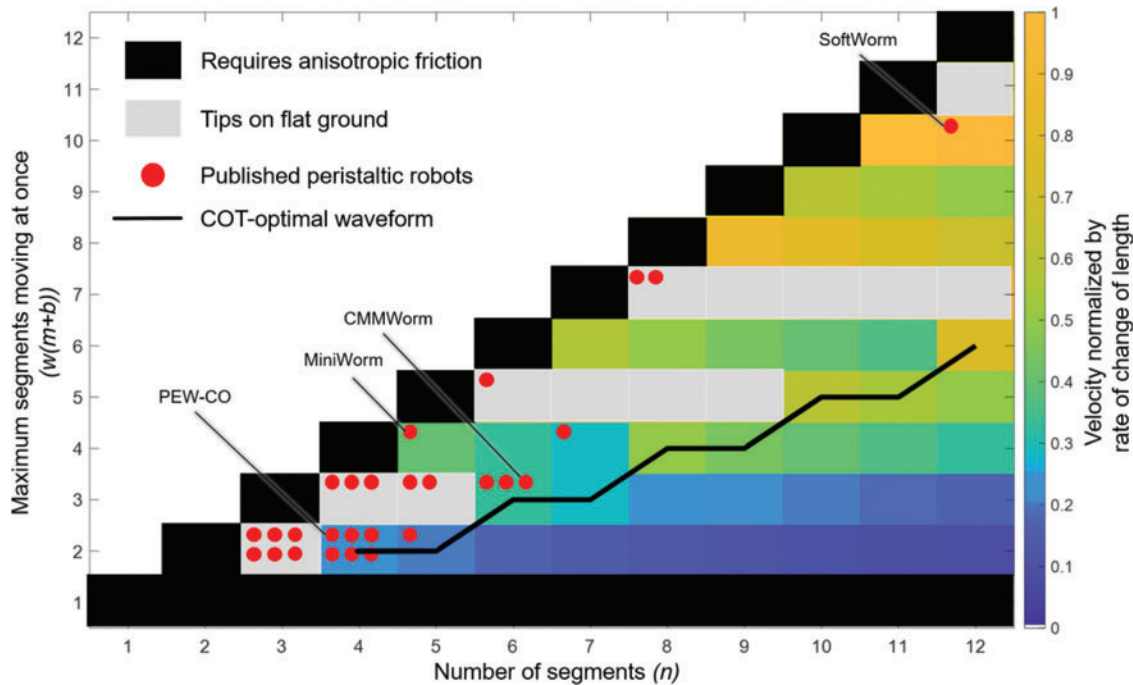


FIG. 9. This plot shows the different velocities that can be achieved by changing the number of moving segments. *Gray boxes* indicate waveforms where the cantilevered segments will tip on flat ground as the number of moving segments in a single wave is more than half the total number of segments. Robots moving more than half their segments can be designed to operate in constrained environments (e.g., pipes), which allows them to achieve traction uniformly along their surface area, thereby preventing them from tipping. *Black boxes* indicate that locomotion will require anisotropic friction. The *black line* is the energy-optimized waveform. Peristaltic robots in existing literature are indicated by *red dots*. For example, *red dots* for number of segments $n=6$ and maximum segments moving at once $w(m+b)=3$, are our robots, CMMWorm,¹⁷ CMMWorm-S,¹⁴ and FabricWorm.⁹⁴ Note: in those cases, in which the ratio of moving to anchoring segments is not constant, that is, complete transition method (Fig. 6AI, III), we consider the ratio of maximum number of moving segments to minimum number of anchoring segments. Note: References for robots mentioned as [number of segments (n), maximum segments moving at once ($w(m+b)$)]; [3,2],^{8,42,43,51,56,87} [4,2],^{50,58,69,85,88,92} [5,2],⁹⁷ [4,3],^{3,80,99} [5,3],^{41,94} [6,3],^{14,17,94} [5,4],⁵⁴ [7,4],⁸³ [6,5],⁵⁹ [8,7],^{78,86} [12,10].¹⁵ Color images are available online.

Conclusions and Discussion

After characterizing >50 worm robot designs (see examples in Fig. 1),^{78–94} we developed a template model (Fig. 3). Assuming perfect segment control and no slip, the theoretical speed of the idealized model [Eq. (1)] is limited by the rate of extension of a segment and the number of moving segments that can be lifted off the ground. Specifically, radial deformation must exceed the vertical bending of cantilevered moving segments in addition to vertical compression of anchoring segments (Fig. 3C). Waveforms with many moving segments concentrate body weight on a few anchoring segments, which then undergo greater vertical compression, and thus will have to further extend those moving segments so as not to drag on the ground. Similarly, more moving segments will have to be further cantilevered from anchoring segments, and thus will also require greater extension to counteract bending deformation [Eq. (4)]. Approximations are found for each of these bending and compression terms, based on assuming that each segment can be modeled as a uniform thin cylinder of length L , radius R , thickness t , and with anisotropic Young's modulus. The bending term is proportional to $(\frac{R}{L})^{-3}$ and the compression term is proportional to $\frac{R}{L}$ times $\frac{R}{L}$. Since R/L ranges from 0.1 to 1 for the robots in the literature and the thickness must always be less than the radius, the

compression term dominates the overall COT as compared with the bending term.

The model highlights three key design choices for a peristaltic robot. First, a segment structure with a nonzero effective Poisson's ratio is needed, which has been achieved in various ways (Fig. 4). Second, actuators capable of causing longitudinal or circumferential strain are needed. We show that at least nine types of actuators have been used in the literature (Fig. 5). The actuation determines the mass and greatly affects the overall stiffness (Young's modulus) of the robot and also can be characterized by speed and power-to-weight-ratio. Finally, a worm robot requires the choice of a waveform shape for control. Although several different wave types have been used (Fig. 6), we propose a unified characterization based on the number of moving segments per wave, the number of waves, and any bridging segments in the wave (see Table 1 for the complete list of possible examples for $n=6$).

Based on these fundamental concepts, we developed an expression for the required power-to-weight output of the segment actuators [Eq. (7)]. The required power is proportional to velocity, and inversely proportional to Poisson's ratio. Furthermore, the power expression also includes geometric and waveform terms, which means that energetically optimal waveforms can be found for various geometries

(Fig. 7). Thus, such waveforms may provide a guide for future robots, which may increase the number of segments to increase speed or reduce power-to-weight requirements (Fig. 8). Power-optimal waveforms have fewer moving segments and more anchoring segments than speed-optimal waveforms, and most current worm robots are between speed optimal and power optimal curves (Fig. 9). Worm robots with larger numbers of segments will be increasingly possible with improved techniques for fabricating large Poisson's ratio segment structure and with novel actuation materials with high power-to-weight ratios. Measuring electrical power input will be especially important for battery-powered untethered robots.

We note that this analysis does not constrain the Young's modulus to a particular optimum value. This suggests that robots capable of peristaltic locomotion can be made out of any convenient materials, soft or hard. In our experience, it is relatively easier to work with stiffer materials¹⁴ because they tend to be easier to control, but if the actuator power-to-weight ratio is too small, actuation may not be possible. In addition, our analysis does not include specific actuator models, but provides a baseline analysis neglecting nonlinearity of the structure and actuator performance. More accurate models can be implemented to use this framework for a specific robot. While developing a robot, researchers can use the analytical guide developed in this article to calculate waveform properties that might be most efficient given geometrical properties, or can calculate geometrical properties given various waveform properties that might help with the initial design of the structure.

Our analysis also suggests an alternative explanation for the behavior of biological earthworms. Perhaps they have so many anchoring segments (as first measured by Quillin¹⁹) not because of anisotropic friction (as has been previously suggested Alexander¹⁸), but because 60% of segments anchoring is optimal for segments locomoting under gravity. To verify the high percentage of anchoring segments in a dry flat environment, we duplicated these experiments with biological earthworms and found that ~50% of segments were stationary at any given time.

On uneven terrain, sensory feedback is likely to be very important for efficient motion. Although current robots often use feedforward control for gaits, we have shown in simulation that COT can be changed in response to feedback, especially in constrained environments.¹⁶ Biological earthworms have a rich range of sensors and their behavior is dominated by feedback: mechanosensory organs and stretch, touch and pressure receptors along the length of the body allow earthworms to locomote in constrained environments and to burrow.⁹⁵ Although there are many worm-like robots, contact sensing has not been explored for most of them. We have demonstrated that by implementing force sensors along the circumference of the mesh structure of our robot, DiSCo-Worm (Distributed Sensing Compliant Worm robot), slip can be reduced while moving in constrained environments.²⁹ However, the use of traditional sensors such as force sensitive resistors, stretch sensors, and inertial measurement units hinder the deformable characteristics of soft robots. Therefore, researchers are developing soft sensors⁹⁶ and sensors that are embedded within soft materials that will allow the structure to retain its flexibility while achieving accurate control.

Future worm robots are needed especially for confined spaces, a challenging terrain for other types of robots. The anchoring segments may need to take advantage of not only more than just radial expansion but also perhaps anisotropic friction or a changing friction coefficient.⁵⁷ The robots will also need to have responsive turning behaviors to climb over and around obstacles. The body stiffness may be critical for terrain adaptation or it may be secondary to other environment-specific design criteria. There remain many design challenges for future study in making soft robots smaller, more autonomous and more responsive—and ultimately more like biological earthworms.

Acknowledgement

The authors thank Kyle Golobish for support in conducting robot experiments.

Author Disclosure Statement

No competing financial interests exist.

Funding Information

This material is based upon study supported by the National Science Foundation under grant No. NSF #1743475 and CRII: RI: Responsive movement primitives for soft robot control, award #1850168.

References

1. Trimmer BA, Takesian AE, Sweet BM, *et al.* Caterpillar locomotion: A new model for soft-bodied climbing and burrowing robots. In: 7th International Symposium on Technology and the Mine Problem, vol. 1, pp. 1–10. Monterey, CA: Mine Warfare Association, 2006.
2. Bertetto AM, Ruggiu M. In-pipe inch-worm pneumatic flexible robot. In: 2001 IEEE/ASME International Conference on Advanced Intelligent Mechatronics. Proceedings (Cat. No. 01TH8556), vol. 2, Como, Italy: IEEE, 2001, pp. 1226–1231.
3. Omori H, Nakamura T, Yada T. An underground explorer robot based on peristaltic crawling of earthworms. *Ind Robot Int J* 2009;36:358–364.
4. Tanaka T, Harigaya K, Nakamura T. Development of a peristaltic crawling robot for long-distance inspection of sewer pipes. In: 2014 IEEE/ASME International Conference on Advanced Intelligent Mechatronics, Besacon, France: IEEE, 2014, pp. 1552–1557.
5. Ikeuchi M, Nakamura T, Matsubara D. October. Development of an in-pipe inspection robot for narrow pipes and elbows using pneumatic artificial muscles. In: 2012 IEEE/RSJ International Conference on Intelligent Robots and Systems, Vilamoura, Portugal: IEEE, 2012, pp. 926–931.
6. Harigaya K, Adachi K, Yanagida T, *et al.* Development of a peristaltic crawling robot for sewer pipe inspection. In: 2013 IEEE International Conference on Mechatronics (ICM), Vicenza, Italy: IEEE, 2013, pp. 267–272.
7. Dario P, Ciarletta P, Menciassi A, *et al.* Modeling and experimental validation of the locomotion of endoscopic robots in the colon. *Int J Robot Res* 2004;23:549–556.
8. Mangan EV, Kingsley DA, Quinn RD, *et al.* Development of a peristaltic endoscope. In: Proceedings 2002 IEEE International Conference on Robotics and Automation (Cat. No. 02CH37292), vol. 1, Washington, DC: IEEE, 2002, pp. 347–352.

9. Wang K, Yan G. Micro robot prototype for colonoscopy and in vitro experiments. *J Med Eng Technol* 2007;31:24–28.
10. Gjorgjieva J, Berni J, Evers JF, *et al.* Neural circuits for peristaltic wave propagation in crawling *Drosophila* larvae: Analysis and modeling. *Front Comput Neurosci* 2013;7:24.
11. Zoran MJ, Drewes CD. The rapid tail withdrawal reflex of the tubificid worm, *Branchiura sowerbyi*. *J Exp Biol* 1988; 137:487–500.
12. Albrecht DR, Bargmann CI. High-content behavioral analysis of *Caenorhabditis elegans* in precise spatiotemporal chemical environments. *Nat Methods* 2011;8:599.
13. Kim B, Lee MG, Lee YP, *et al.* An earthworm-like micro robot using shape memory alloy actuator. *Sens Actuata A Phys* 2006;125:429–437.
14. Kandhari A, Huang Y, Daltorio KA, *et al.* Body stiffness in orthogonal directions oppositely affects worm-like robot turning and straight-line locomotion. *Bioinspir Biomim* 2018;13:026003.
15. Boxerbaum AS, Shaw KM, Chiel HJ, *et al.* Continuous wave peristaltic motion in a robot. *Int J Robot Res* 2012;31: 302–318.
16. Daltorio KA, Boxerbaum AS, Horchler AD, *et al.* Efficient worm-like locomotion: Slip and control of soft-bodied peristaltic robots. *Bioinspir Biomim* 2013;8:035003.
17. Horchler AD, Kandhari A, Daltorio KA, *et al.* Peristaltic locomotion of a modular mesh-based worm robot: Precision, compliance, and friction. *Soft Robot* 2015;2:135–145.
18. Alexander RM. *Principles of Animal Locomotion*. Princeton, NJ: Princeton University Press, 2003.
19. Quillin KJ. Kinematic scaling of locomotion by hydrostatic animals: Ontogeny of peristaltic crawling by the earthworm *Lumbricus terrestris*. *J Exp Biol* 1999;202:661–674.
20. Chapman G. Of the movement of worms. *J Exp Biol* 1950; 27:29–39.
21. Chiel HJ, Crago P, Mansour JM, *et al.* Biomechanics of a muscular hydrostat: A model of lapping by a reptilian tongue. *Biol Cybern* 1992;67:403–415.
22. Jiang Z, Xu J. The optimal locomotion of a self-propelled worm actuated by two square waves. *Micromachines* 2017;8:364.
23. Fang H, Wang C, Li S, *et al.* A comprehensive study on the locomotion characteristics of a metameric earthworm-like robot. *Multibody Syst Dynam* 2015;35:153–177.
24. Gmitterko A, Kelemen M, Virgala I, *et al.* Modeling of a snake-like robot rectilinear motion and requirements for its actuators. In: 2011 15th IEEE International Conference on Intelligent Engineering Systems, Poprad, Slovakia: IEEE, 2011, pp. 91–94.
25. Niebur E, Erdős P. Theory of the locomotion of nematodes: Dynamics of undulatory progression on a surface. *Biophys J* 1991;60:1132–1146.
26. Boyle JH, Berri S, Cohen N. Gait modulation in *C. elegans*: An integrated neuromechanical model. *Front Comput Neurosci* 2012;6:10.
27. Schwebke S, Behn C. Worm-like robotic systems: Generation, analysis and shift of gaits using adaptive control. *Artif Intell Res* 2013;2:12–35.
28. Tanaka Y, Ito K, Nakagaki T, Kobayashi, R. Mechanics of peristaltic locomotion and role of anchoring. *J Roy Soc Interface* 2012;9:222–233.
29. Kandhari A, Wang Y, Chiel HJ, *et al.* Turning in worm-like robots: The geometry of slip elimination suggests non-periodic waves. *Soft Robot* 2019;6:560–577.
30. Lee C, Kim M, Kim YJ, *et al.* Soft robot review. *Int J Control Autom Syst* 2017;15:3–15.
31. Rus D, Tolley MT. Design, fabrication and control of soft robots. *Nature* 2015;521:467–475.
32. Kim S, Laschi C, Trimmer B. Soft robotics: A bio-inspired evolution in robotics. *Trends Biotechnol* 2013;31: 287–294.
33. Gray J, Lissmann HW. Studies In animal locomotion: VII. Locomotory reflexes in the earthworm. *J Exp Biol* 1938;15: 506–517.
34. Full RJ, Koditschek DE. Templates and anchors: Neuro-mechanical hypotheses of legged locomotion on land. *J Exp Biol* 1999;202:3325–3332.
35. Lin HT, Trimmer B. The substrate as a skeleton: ground reaction forces from a soft-bodied legged animal. *J Exp Biol* 2010;213:1133–1142.
36. Hawkes EW, Blumenschein LH, Greer JD, *et al.* A soft robot that navigates its environment through growth. *Sci Robot* 2017;2:p.eaan3028.
37. Ijspeert AJ, Crespi A, Ryczko D, *et al.* From swimming to walking with a salamander robot driven by a spinal cord model. *Science* 2007;315:1416–1420.
38. Marvi H, Bridges J, Hu DL. Snakes mimic earthworms: Propulsion using rectilinear travelling waves. *J R Soc Interface* 2013;10:20130188.
39. Onal CD, Rus D. A modular approach to soft robots. In *Proceedings of the IEEE RAS and EMBS International Conference on Biomedical Robotics and Biomechanics*, Rome, Italy: IEEE, 2012, pp. 1038–1045.
40. Kandhari A, Stover MC, Jayachandran PR, *et al.* Distributed sensing for soft worm robot reduces slip for locomotion in confined environments. In: *Conference on Biomimetic and Biohybrid Systems*, pp. 236–248. Cham: Springer, 2018.
41. Seok S, Onal CD, Cho KJ, *et al.* Meshworm: A peristaltic soft robot with antagonistic nickel titanium coil actuators. *IEEE/ASME Trans Mech* 2012;18:1485–1497.
42. Ono M, Kato S. A study of an earthworm type inspection robot movable in long pipes. *Int J Adv Robot Syst* 2010;7:2.
43. Wang K, Wang Z, Zhou Y, *et al.* Squirm robot with full bellow skin for colonoscopy. In: 2010 IEEE International Conference on Robotics and Biomimetics, Tianjin, China: IEEE, 2010, pp. 53–57.
44. Wang K, Ge Y, Jin X. A micro soft robot using inner air transferring for colonoscopy. In: 2013 IEEE International Conference on Robotics and Biomimetics (ROBIO), Shenzhen, China: IEEE, 2013, pp. 1556–1561.
45. Calderón AA, Ugalde JC, Zagal JC, *et al.* Design, fabrication and control of a multi-material-multi-actuator soft robot inspired by burrowing worms. In: 2016 IEEE International Conference on Robotics and Biomimetics (ROBIO), Qingdao, China: IEEE, 2016, pp. 31–38.
46. Zhang X, Pan T, Heung HL, *et al.* A biomimetic soft robot for inspecting pipeline with significant diameter variation. In: 2018 IEEE/RSJ International Conference on Intelligent Robots and Systems (IROS), Madrid, Spain: IEEE, 2018, pp. 7486–7491.
47. Kamata M, Tachibana K, Tanise Y, *et al.* Proposal of one-inch pipe inspection robot “PI-RO I.” In: 2018 7th IEEE International Conference on Biomedical Robotics and Biomechanics (Biorob), Enschede, The Netherlands: IEEE, 2018, pp. 1315–1320.
48. Adams W, Sridar S, Thalman CM, *et al.* Water pipe robot utilizing soft inflatable actuators. In: 2018 IEEE International Conference on Soft Robotics (RoboSoft), Livorno, Italy: IEEE, 2018, pp. 321–326.

49. Joey ZG, Calderón AA, Chang L, *et al.* An earthworm-inspired friction-controlled soft robot capable of bidirectional locomotion. *Bioinspir Biomim* 2019;14:036004.
50. Nakamura T, Iwanaga T. Locomotion strategy for a peristaltic crawling robot in a 2-dimensional space. In: 2008 IEEE International Conference on Robotics and Automation, Pasadena, CA: IEEE, 2008, pp. 238–243.
51. Onal CD, Wood RJ, Rus D. An origami-inspired approach to worm robots. *IEEE/ASME Trans Mech* 2012;18:430–438.
52. Evans KE, Alderson A. Auxetic materials: Functional materials and structures from lateral thinking!. *Adv Mater* 2000;12:617–628.
53. Trivedi D, Rahn CD, Kier WM, *et al.* Soft robotics: Biological inspiration, state of the art, and future research. *Appl Bionics Biomech* 2008;5:99–117.
54. Andersen KB, Kandhari A, Chiel HJ, *et al.* A nitinol-actuated worm robot bends for turning and climbing obstacles. In *Conference on Biomimetic and Biohybrid Systems*, pp. 6–10. Cham: Springer, 2018.
55. Zarrouk D, Sharf I, Shoham M. Analysis of earthworm-like robotic locomotion on compliant surfaces. In: 2010 IEEE International Conference on Robotics and Automation, Anchorage, AK: IEEE, 2010, pp. 1574–1579.
56. Winstone B, Pipe T, Melhuish C, *et al.* Single motor actuated peristaltic wave generator for a soft bodied worm robot. In: 2016 6th IEEE International Conference on Biomedical Robotics and Biomechanics (BioRob), Singapore: IEEE, 2016, pp. 449–456.
57. Liu B, Ozkan-Aydin Y, Goldman DI, *et al.* Kirigami skin improves soft earthworm robot anchoring and locomotion under cohesive soil. In: 2019 2nd IEEE International Conference on Soft Robotics (RoboSoft), Seoul, South Korea: IEEE, 2019, pp. 828–833.
58. Qi Q, Teng Y, Li X. Design and characteristic study of a pneumatically actuated earthworm-like soft robot. In: 2015 International Conference on Fluid Power and Mechatronics (FPM), Harbin, China: IEEE, 2015, pp. 435–439.
59. Fang H, Zhang Y, Wang KW. Origami-based earthworm-like locomotion robots. *Bioinspir Biomim* 2017;12:065003.
60. Aydin YO, Molnar JL, Goldman DI, *et al.* Design of a soft robophysical earthworm model. In: 2018 IEEE International Conference on Soft Robotics (RoboSoft), Livorno, Italy: IEEE, 2018, pp. 83–87.
61. Mano Y, Ishikawa R, Yamada Y, *et al.* Development of contraction force control system of peristaltic crawling robot for sewer pipe inspection. In: 2018 IEEE/ASME International Conference on Advanced Intelligent Mechatronics (AIM), Auckland, New Zealand: IEEE, 2018, pp. 936–941.
62. Ortiz D, Gravish N, Tolley MT. Soft robot actuation strategies for locomotion in granular substrates. *IEEE Robot Autom Lett* 2019;4:2630–2636.
63. Wehner M, Tolley MT, Mengüç Y, *et al.* Pneumatic energy sources for autonomous and wearable soft robotics. *Soft Robot* 2014;1:263–274.
64. Antonelli MG, Beomonte Zobel P, Durante F, *et al.* Numerical modelling and experimental validation of a McKibben pneumatic muscle actuator. *J Intell Mater Syst Struct* 2017;28:2737–2748.
65. Vaidyanathan R, Chiel HJ, Quinn RD. A hydrostatic robot for marine applications. *Robot Auton Syst* 2000;30:103–113.
66. Elango N, Faudzi AAM. A review article: Investigations on soft materials for soft robot manipulations. *Int J Adv Manuf Technol* 2015;80:1027–1037.
67. Hines L, Petersen K, Lum GZ, *et al.* Soft actuators for small-scale robotics. *Adv Mater* 2017;29:1603483.
68. Miriyev A, Stack K, Lipson H. Soft material for soft actuators. *Nat Commun* 2017;8:596.
69. Zhao J, Niu J, Liu L, *et al.* A soft creeping robot actuated by dielectric elastomer. In *Electroactive Polymer Actuators and Devices (EAPAD) 2014*, vol. 9056, San Diego, CA: International Society for Optics and Photonics, 2014, p. 905608.
70. Mikanojima T, Maeda S, Hara Y, *et al.* Peristaltic motion of tubular gel driven by acid-autocatalytic reaction. *Adv Robot* 2014;28:457–465.
71. Webster-Wood VA, Akkus O, Gurkan UA, *et al.* Organismal engineering: Toward a robotic taxonomic key for devices using organic materials. *Sci Robot* 2017;2:eaap9281.
72. Okay O. General properties of hydrogels. In: Urban G. (Ed). *Hydrogel Sensors and Actuators*, Berlin, Heidelberg: Springer, 2009, pp. 1–14.
73. Mirfakhrai T, Madden JD, Baughman RH. Polymer artificial muscles. *Mater Today* 2007;10:30–38.
74. White TJ, Broer DJ. Programmable and adaptive mechanics with liquid crystal polymer networks and elastomers. *Nat Mater* 2015;14:1087–1098.
75. Liu C, Qin H, Mather PT. Review of progress in shape-memory polymers. *J Mater Chem* 2007;17:1543–1558.
76. Tolley MT, Shepherd RF, Mosadegh B, *et al.* A resilient, untethered soft robot. *Soft Robot* 2014;1:213–223.
77. Michal BT, McKenzie BM, Felder SE, *et al.* Metallo-, thermo-, and photoresponsive shape memory and actuating liquid crystalline elastomers. *Macromolecules* 2015;48:3239–3246.
78. Saga N, Nakamura T. Development of a peristaltic crawling robot using magnetic fluid on the basis of the locomotion mechanism of an earthworm. In: *Smart Structures, Devices, and Systems*, vol. 4935, Melbourne, Australia: International Society for Optics and Photonics, 2002, pp. 369–378.
79. Chi D, Yan G. October. Earthworm-based miniature robot for intestinal inspection. In: *Micromachining and Microfabrication Process Technology and Devices*, vol. 4601, Nanjing, China, pp. 396–401. International Society for Optics and Photonics, 2001.
80. Mencias A, Gorini S, Pernorio G, *et al.* Design, fabrication and performances of a biomimetic robotic earthworm. In 2004 IEEE International Conference on Robotics and Biomimetics, Shenyang, China: IEEE, 2004, pp. 274–278.
81. Kim B, Park S, Jee CY, *et al.* An earthworm-like locomotive mechanism for capsule endoscopes. In 2005 IEEE/RSJ International Conference on Intelligent Robots and Systems, Edmonton, Alberta, Canada: IEEE, 2005, pp. 2997–3002.
82. Jung K, Koo JC, Lee YK, *et al.* Artificial annelid robot driven by soft actuators. *Bioinspir Biomim* 2007;2:S42.
83. Omori H, Hayakawa T, Nakamura T. Locomotion and turning patterns of a peristaltic crawling earthworm robot composed of flexible units. In: 2008 IEEE/RSJ International Conference on Intelligent Robots and Systems, Nice, France: IEEE, 2008, pp. 1630–1635.
84. Zhou M, Tao Y, Cheng L, *et al.* A biomimetic earthworm-like micro robot using nut-type piezoelectric motor. In: International Conference on Intelligent Robotics and Applications, pp. 129–135. Berlin, Heidelberg: Springer, 2013.
85. Manwell T, Vitek T, Ranzani T, *et al.* Elastic mesh braided worm robot for locomotive endoscopy. In: 2014 36th Annual International Conference of the IEEE Engineering in Medicine and Biology Society, Chicago, IL: IEEE, 2014, pp. 848–851.

86. Fang H, Wang C, Li S, *et al.* Design and experimental gait analysis of a multi-segment in-pipe robot inspired by earthworm's peristaltic locomotion. In: *Bioinspiration, Biomimetics, and Bioreplication 2014*, vol. 9055, San Diego, CA: International Society for Optics and Photonics, 2014, p. 90550H.
87. Zhang K, Qiu C, Dai JS. Helical kirigami-enabled centimeter-scale worm robot with shape-memory-alloy linear actuators. *J Mech Robot* 2015;7:021014.
88. Sun Z, Yamauchi Y, Araoka F, *et al.* An anisotropic hydrogel actuator enabling earthworm-like directed peristaltic crawling. *Angew Chem* 2018;130:15998–16002.
89. Manwell T, Guo B, Back J, *et al.* Bioinspired setae for soft worm robot locomotion. In: *2018 IEEE International Conference on Soft Robotics (RoboSoft)*, Livorno, Italy: IEEE, 2018, pp. 54–59.
90. Tadami N, Isaka K, Nakatake T, *et al.* Underwater excavation by excavation robot equipped with propulsion unit based on earthworm setae. In: *2018 IEEE International Conference on Robotics and Biomimetics (ROBIO)*, Kuala Lumpur, Malaysia: IEEE, 2018, pp. 51–58.
91. Qin L, Liang X, Huang H, *et al.* A versatile soft crawling robot with rapid locomotion. *Soft Robot* 2019;6:455–467.
92. Yang W, Zhang W. A worm-inspired robot flexibly steering on horizontal and vertical surfaces. *Appl Sci* 2019;9:2168.
93. Yeh CY, Chou SC, Huang HW, *et al.* Tube-crawling soft robots driven by multistable buckling mechanics. *Extreme Mech Lett* 2019;26:61–68.
94. Kandhari A, Mehringer A, Chiel HJ, *et al.* Design and actuation of a fabric-based worm-like robot. *Biomimetics* 2019;4:1.
95. Mill P. Recent developments in earthworm neurobiology in *Comp. Biochem Physiol* 1982;12:107–115.
96. Park YL, Chen BR, Wood RJ. Design and fabrication of soft artificial skin using embedded microchannels and liquid conductors. *IEEE Sens J* 2012;12:2711–2718.
97. Nemitz MP, Mihaylov P, Barraclough TW, *et al.* Using voice coils to actuate modular soft robots: Wormbot, an example. *Soft Robot* 2016;3:198–204.
98. Yao YY, Liu J. A polarized liquid metal worm squeezing across a localized irregular gap. *RSC Adv* 2017;7:11049–11056.
99. Saga N, Nakamura T, Ueda S. Study on peristaltic crawling robot using artificial muscle actuator. In *Proceedings 2003 IEEE/ASME International Conference on Advanced Intelligent Mechatronics (AIM 2003)*, vol. 1, Kobe, Japan: IEEE, 2003, pp. 679–684.

Address correspondence to:

Kathryn Daltorio

*Department of Mechanical and Aerospace Engineering
Case Western Reserve University
Glennan Building, Room 410
10900 Euclid Avenue
Cleveland, OH 44106-7222
USA*

E-mail: kati@case.edu

Appendices I and II

Appendix I. Velocity Calculation

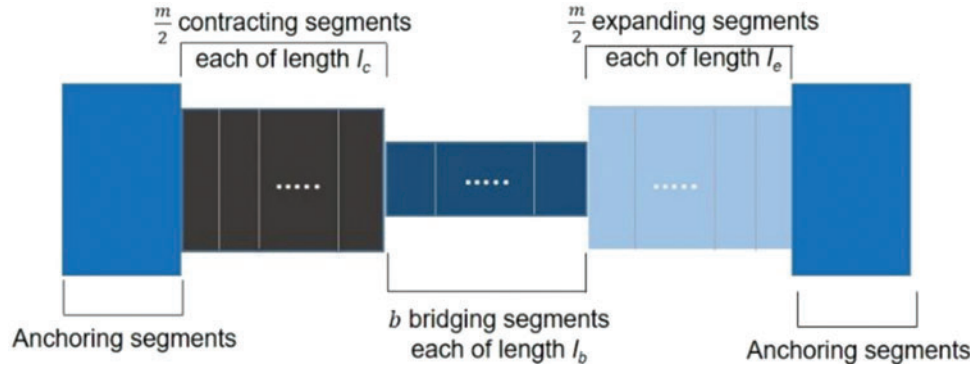
Let there be a total of n segments, and between two anchoring let there be a total of $m/2$ circumferentially

contracting segments, b bridged segments, and $m/2$ circumferentially expanding segment. The mass of each segment is m_{seg} (Fig. A1).

The position of the center of mass (COM) is defined as

$$\begin{aligned}
 COM = & \frac{\left[\frac{1}{2}L_c + \frac{3}{2}L_c + \dots + \frac{(2(\frac{m}{2}) - 1)}{2}L_c \right] + \left[\left(\frac{m}{2}L_c + \frac{1}{2}L_b \right) + \left(\frac{m}{2}L_c + \frac{3}{2}L_b \right) + \dots + \left(\frac{m}{2}L_c + \frac{(2b - 1)}{2}L_b \right) \right] + \left[\left(\frac{m}{2}L_c + bL_b + \frac{1}{2}L_e \right) + \left(\frac{m}{2}L_c + bL_b + \frac{3}{2}L_e \right) + \left(\frac{m}{2}L_c + bL_b + \frac{(2(\frac{m}{2}) - 1)}{2}L_e \right) \right]}{n}
 \end{aligned} \quad (A1.1)$$

(Appendix continues →)



APPENDIX FIG A1. Schematic depicting a total of n segments, where a total of $m/2$ segments are contracting in diameter, $m/2$ segments are expanding in diameter and b segments are bridged between the contracting and expanding segments. The length of each contracting segments is l_c , the length of the expanding segments is l_e , and the length of the bridged segment is l_b . For locomotion without slip, the anchoring segments are at their maximum diameter and do not move. Color images are available online.

Taking derivatives of the length L with respect to time, the velocity of the COM is

$$v_{COM} = \frac{\left[\frac{1}{2}\dot{L}_c + \frac{3}{2}\dot{L}_c + \dots + \frac{(2(\frac{m}{2})-1)}{2}\dot{L}_c \right] + \left[\left(\frac{m}{2}\dot{L}_c + \frac{1}{2}\dot{L}_b \right) + \left(\frac{m}{2}\dot{L}_c + \frac{3}{2}\dot{L}_b \right) + \dots + \left(\frac{m}{2}\dot{L}_c + \frac{(2b-1)}{2}\dot{L}_b \right) \right] + \left[\left(\frac{m}{2}\dot{L}_c + b\dot{L}_b + \frac{1}{2}\dot{L}_e \right) + \left(\frac{m}{2}\dot{L}_c + b\dot{L}_b + \frac{3}{2}\dot{L}_e \right) + \left(\frac{m}{2}\dot{L}_c + b\dot{L}_b + \frac{(2(\frac{m}{2})-1)}{2}\dot{L}_e \right) \right]}{n} \quad (\text{AI.2})$$

The length of the bridged segment does not change over time and for our case the rate of circumferential expansion is equal to the rate of circumferential contractions, which implies that

$$\therefore \dot{L}_c = -\dot{L}_e = \dot{L} \quad (\text{AI.3})$$

Simplifying Equation (2), we get

$$v_{com} = \frac{\left[\frac{1}{2}\dot{L}_c + \frac{3}{2}\dot{L}_c + \dots + \frac{(2(\frac{m}{2})-1)}{2}\dot{L}_c \right] + \left[\left(\frac{m}{2}\dot{L}_c \right) + \left(\frac{m}{2}\dot{L}_c \right) + \dots + \left(\frac{m}{2}\dot{L}_c \right) \right] + \left[\left(\frac{m}{2}\dot{L}_c - \frac{1}{2}\dot{L}_c \right) + \left(\frac{m}{2}\dot{L}_c - \frac{3}{2}\dot{L}_c \right) + \left(\frac{m}{2}\dot{L}_c - \frac{(2(\frac{m}{2})-1)}{2}\dot{L}_c \right) \right]}{n} \quad (\text{AI.4})$$

$$v_{COM} = \frac{b \left[\frac{m}{2} \right] \dot{L} + \frac{m}{2} \left[\left(\frac{m}{2} \right) \dot{L} \right]}{n} \quad (\text{AI.5})$$

$$v_{COM} = \frac{m(m+2b)}{4n} \dot{L} \quad (\text{AI.6})$$

For multiple waves traveling within the body, anchoring segments would not move and the ideal velocity of the body is multiplied by the number of waves.

$$\therefore v_{ideal} = \frac{wm(m+2b)}{4n} \dot{L} \quad (\text{AI.7})$$

Appendix II. COT Calculation

$$|\Delta R| > y + d, \quad (\text{AII.1})$$

where y is deformation due to cantilever of segments

$$y = \frac{(m+b)^4 m_{seg} g L^3}{8EI} \quad (\text{AII.2})$$

I is the moment of inertia for a thin cylinder

$$I = \pi R^3 t \quad (\text{AII.3})$$

$$\therefore y = \frac{(m+b)^4 m_{seg} g L^3}{8E\pi R^3 t} \quad (\text{AII.4})$$

(Appendix continues \rightarrow)

d is the compression on the anchoring segments due to the weight of the entire structure

$$d = \frac{m_{\text{seg}} g n}{(n - w(m + b)) 24Et} \frac{(R)^3}{24Et}. \quad (\text{AII.5})$$

I is the moment of inertia for a thin rod, which is

$$I = \frac{1}{12} L t^3. \quad (\text{AII.6})$$

$$\therefore d = \frac{m_{\text{seg}} g n}{(n - w(m + b)) 2E(Lt^3)}. \quad (\text{AII.7})$$

For the case of small deformations, ΔR can be simplified as

$$|\Delta R| \approx \vartheta R \frac{\Delta l}{L}. \quad (\text{AII.8})$$

$$\vartheta R \frac{\Delta l}{L} > \frac{(m + b)^4 m_{\text{seg}} g L^3}{8E\pi R^3 t} + \frac{m_{\text{seg}} g n}{(n - w(m + b)) 2E(Lt^3)}. \quad (\text{AII.9})$$

$$\vartheta R \frac{\Delta l}{L} > \frac{m_{\text{seg}} g}{Et} \left[\frac{(m + b)^4 L^3}{8\pi R^3} + \frac{n}{(n - w(m + b)) 2(Lt^2)} \right]. \quad (\text{AII.10})$$

$$\frac{\vartheta R E t \Delta l}{m_{\text{seg}} g L} > \left[\frac{(m + b)^4 L^3}{8\pi R^3} + \frac{n}{(n - w(m + b)) 2(Lt^2)} \right]. \quad (\text{AII.11})$$

Note: E in Equation (AII.11) is Young's modulus along the circumferential axis, and is denoted as E_c in the following steps.

Energy in a linear elastic structure

$$U = \frac{1}{2} V E_t \varepsilon^2, \quad (\text{AII.12})$$

where V is volume and E_t is Young's modulus along the longitudinal axis.

Assuming P to be the ratio of power to weight, P can be written as

$$P = \frac{V E_t \varepsilon^2}{2 m_{\text{seg}} g \Delta T}. \quad (\text{AII.13})$$

Substituting E into the LHS of Equation (AII.11) and substituting V for a thin cylinder = $2\pi R L t$ and $\varepsilon = \Delta l / L$

$$\frac{\vartheta R t \Delta l E_c}{m_{\text{seg}} g L} \frac{2 m_{\text{seg}} g \Delta T P}{V \varepsilon^2 E_t} = \frac{\vartheta R t \Delta l E_c}{m_{\text{seg}} g L} \frac{2 m_{\text{seg}} g \Delta T P L^2}{2 \pi R L t \Delta l^2 E_t} = \frac{\vartheta \Delta T P E_c}{\pi \Delta l E_t}. \quad (\text{AII.14})$$

$$\therefore \frac{\vartheta \Delta T P E_c}{\pi \Delta l E_t} > \left[\frac{(m + b)^4 L^3}{8\pi R^3} + \frac{n}{(n - w(m + b)) 2(Lt^2)} \right]. \quad (\text{AII.15})$$

Multiplying and dividing the RHS by V_{ideal}

$$v_{\text{ideal}} = \frac{w m (m + 2b)}{4n} \dot{L}. \quad (\text{AII.16})$$

$$\frac{\vartheta P E_c}{\pi L E_t} > \left[\frac{(m + b)^4 L^3}{8\pi R^3} + \frac{n}{(n - w(m + b)) 2(Lt^2)} \right] \left[\frac{v_{\text{ideal}}}{\frac{w m (m + 2b)}{4n} \dot{L}} \right]. \quad (\text{AII.17})$$

$$\frac{\vartheta P}{v_{\text{ideal}}} > \frac{1}{E_c / E_t} \left[\frac{n(m + b)^4 L^3}{2R^3} + \frac{2\pi n^2}{(n - w(m + b)) (Lt^2)} \right] \left[\frac{1}{w m (m + 2b)} \right]. \quad (\text{AII.18})$$

$$COT > \frac{1}{\vartheta \frac{E_c}{E_t}} \left[\frac{n(m + b)^4}{2w m (m + 2b)} \left(\frac{R}{L} \right)^{-3} + \frac{2\pi n^2}{w m (m + 2b) (n - w(m + b))} \left(\frac{R}{L} \right) \left(\frac{R}{t} \right)^2 \right]. \quad (\text{AII.19})$$